α–Ag$_2$WO$_4$ under microwave, electron beam and femtosecond laser irradiations: Unveiling the relationship between morphology and photoluminescence emissions

Mayara Mondego Teixeira,‡[a*] Lílian Cruz Santos,‡[a] Ana Cristina Mora Tello,‡[a*] Priscila Barros Almeida,‡[a] Jussara Soares da Silva,‡[a] Letícia Laier,‡[b], Lourdes Gracia,[c,d] Marcio Daldin Teodoro,[e] Luís Fernando da Silva,[e] Juan Andrés[c] and Elson Longo[a*]

[a]Departamento de Química, CDMF, Universidade Federal de São Carlos, 13565-905 São Carlos, São Paulo, Brazil.

[b]Laboratório Interdisciplinar em Cerâmica, Departamento de Físico-Química, Instituto de Química, UNESP, 14800-900, Araraquara, São Paulo, Brazil.

[c]Departamento de Química Física i Analítica, University Jaume I, 12071, Castelló de la Plana, Spain.

[d]Departamento de Química Física, Universitat de València, 46100, Burjassot, Spain.

[e]Departamento de Física, Universidade Federal de São Carlos, 13565-905, São Carlos, São Paulo, Brazil.

‡ These authors contributed equally to this work

Corresponding Author: elson.liec@gmail.com; mayaramondego.ufma@gmail.com; anacmora@gmail.com

ABSTRACT

In this study, the α-Ag$_2$WO$_4$ samples were successfully synthesized combined two methods, co-precipitation and microwave-assisted hydrothermal. Later, two different irradiation processes: electron beam and femtosecond laser are applied. Unit cell changes were shown by X-ray measurements and Rietveld analysis and compared with the results obtained for first-principle calculations. The formation of oxygen vacancies on the surface of the particles after the irradiation process was revealed by XPS measurements. Electron beam and femtosecond laser irradiations were found to cause expansion of the unit cell, form oxygen vacancies on the surface, change the angle and distance between O–Ag and O–W bonds, and modify the particle morphology to rod-, cube- and sphere-like. The XANES measurements confirm that the local order of the W atoms is maintained along the different irradiation processes. Based on the theoretical anlaysis of surfaces investigation and Wulff construction, the contribution of (010) and (101) surfaces at the emission centers in 550 and 733 nm associated to the PL spectrum of α–Ag$_2$WO$_4$, was established.

1. INTRODUCTION

Recently, alpha-silver tungstate (α–Ag_2WO_4) has attracted increasing attention from scientists due to its several unique characteristics. Among them, we can cite its nontoxicity [1–3], photoluminescence properties [4,5], and photocatalytic applications [1–6]. These properties can be improved according to the obtained morphologies by different synthesis methodologies, such as simple co-precipitation [6–8], conventional hydrothermal [9,10], or microwave-assisted hydrothermal (MAH) method [11].

When it comes to time-saving synthesis, the MAH method is considerably more advantageous than other methodologies [12–15] since the use of microwave irradiation triggers different processes between the forming clusters and the electromagnetic waves, culminating in the formation of more oxygen defects and more structural/electronic disorder effects in the structure of the material [16].

The properties derived from the interaction between electromagnetic waves and the material have been studied for several decades. It is known that the characterization of structure or property responses of the material to these stimuli from the surrounding environment plays a key role in the understanding and rationalization of the structure-property relationship function in modern science and engineering [17,18]. In a recent study conducted by our group, α–Ag_2WO_4 was obtained by the MAH method. It was observed that the photoluminescence of these samples migrated from red to blue, according to the morphology and structural disorder presented [19].

It is also known that factors such as temperature, time of synthesis, and presence of surfactants among others can alter the lattice structural properties of α–Ag_2WO_4 as well [6,20,21]. Regarding the influence of time of exposure to MAH, in a recent study performed by Laier et al. (2020) [20] both experimental and computational results revealed that at certain times of operation of the MAH system it was possible to obtain

samples with the highest active surface composition since they showed a higher density of broken bonds and greater surface energy. The irradiation of electron beam and femtosecond laser on the α–Ag$_2$WO$_4$ structure has attracted attention [10,11,22–32], where the main focus is to elucidate the mechanism of growth of Ag nanoparticles on the surface α–Ag$_2$WO$_4$ and the effects on the photoluminescence (PL) emissions [22, 32-35].

In this work, we have tried to understand the phenomena provoked by the interaction between α–Ag$_2$WO$_4$ and electron beam and femtosecond laser irradiation, which were found to be able to promote changes in the lattice parameters, structure, and morphology of the crystal. All of these changes alter the material properties, for example, its electronic and magnetic properties, [22,36,37], PL emissions, and consequently its physical, chemical and/or biological applications [6,20,31,34,38]. Therefore, it is possible to adjust the morphology, lattice, and electronic structures of α–Ag$_2$WO$_4$ materials resulting from these modifications [19,39].

It should be noted that alterations in the lattice structure of the crystal may directly contribute to the variation in the number of vacancies. Once there is a critical correlation among lattice parameters, structural stability, electronic structure, band gap, and photoluminescence properties, it is important to have a broad understanding at the atomic-level of its bulk and surface.

In summary, This article came to increase knowledge about this structure and bring newness through the approach of explaining photoluminescence (PL), showing the surface that contributes to the property. It is well known that PL emission is the concentration of different defects: intrinsic (bulk and surface), extrinsic under interface, and structural order-disorder [32,40]. However, the surface contribution is still little known for the α–Ag$_2$WO$_4$ structure. For this purpose, we synthesized α–Ag$_2$WO$_4$ using the co-precipitation (CP) method, followed by the MAH method as a function of the

synthesis time (2, 4, 8, 16, and 32 min) and electron beam and femtosecond laser irradiations. The crystals were characterized by different structural techniques, and their optical and PL properties were investigated. Theoretical calculations at the density functional theory (DFT) level were performed to obtain atomic information of the electronic structure of the material after irradiation. In addition, to understand the relationship between PL emissions of the α–Ag_2WO_4 exposed surfaces, the corresponding band gap was analyzed. The paper is organized as follows: section 2 describes the experimental procedure (synthesis, characterization, and irradiation methods) and the theoretical method, whereas section 3 shows the results and discussion on the structure, morphology, and optical properties of α–Ag_2WO_4. Finally, we present our main conclusions in section 4.

2. EXPERIMENTAL SECTION

2.1. Synthesis of α-Ag_2WO_4 crystals

The α–Ag_2WO_4 samples were synthesized by the CP method, similar to the description made by Foggi, *et al.* (2017) [41], being considered a volume of 30 mL of ethanol, then kept under continuous stirring for 10 min; the as-obtained sample was denoted as CP. The suspension followed by treatment in the MAH method (**Figure 1a,b**) under the previous studies by [4,5,20,42], considering the treatment times of 2, 4, 8, 16, and 32 min. These samples were denoted as MAH-2, MAH-4, MAH-8, MAH-16, and MAH-32.

2.2. Irradiated samples (EI and FI)

To obtain the irradiated samples, the set of MAH samples were submitted to two different irradiations: electron beam irradiation (EI) (**Figure 1c**) and femtosecond laser

118   irradiation (FI) (**Figure 1d**). The EI process was conducted in a field emission scanning

119   electron microscope (Supra 35-VP; Carl Zeiss – Germany), using an acceleration voltage

120   of 30 kV for 2 minutes, the parameters were selected based on experiments reported in

121   the references [24,28,30]. The samples obtained through this process were denoted as EI-

122   2, EI-4, EI-8, EI-16, and EI-32. Regarding the femtosecond laser irradiation, the

123   procedure is according to Protocol I reported in reference [29], using a titanium/sapphire

124   laser (Femtopower Compact Pro, Femto Lasers) with pulses of 30 fs of full width at half

125   maximum, the wavelength of 800 nm, the repetition rate of 1 kHz and fluence of 60 J/cm^2

126   in diameter of the order of 20 µm. The obtained samples were denoted as FI-2, FI-4, FI-

127   8, FI-16, and FI-32. Experimental characterizations of the samples are in Supplementary

128   Information.

129

130   **Figure 1.**

131

132   **2.3. Model systems and Theoretical Methods**

133   Density functional theory (DFT) calculations were performed with the

134   CRYSTAL17 program [43]. The B3LYP hybrid functional (doi:10.1063/1.464304) was

135   used for described the electron-electron interactions combined with the effective core

136   pseudopotentials (ECP) derived by Apra [44] and Corà [45] which have been chosen for

137   described silver and tungsten, respectively, while the oxygen was described with the 8-

138   411d11G basis set [46]. From the experimental results of Rietveld refinements of the CP

139   sample, we derived a theoretical reference model (***opt*** – α-Ag$_2$WO$_4$) by full optimization

140   of the structural parameters of α–Ag$_2$WO$_4$. The accuracy in the evaluation of the Coulomb

141   and exchange was controlled by a set of tolerances with values of 10^{-8}, 10^{-8}, 10^{-8}, 10^{-8}, and

142   10^{-16}. A total mesh of 125 *k*-points was employed to sample uniformly the irreducible part

of the Brillouin zone. The vibrational modes at the Γ point were calculated by using the numerical second derivates of the total energy. On the other hand, for the set of MAH, EI, and FI samples, only the atomic positions were allow for relax. The relaxed structures were used for the electronic structure calculations. Visualization of the unit cells was performed using the VESTA program [47].

The electronic structure of the (010), (100), (001), (011), (101), and (110) surfaces of α-Ag_2WO_4 were discussed from band gap energy values and the density of states (DOS). Details computationals for the surfaces calculations can be found in previous studies. [48]

The density broken bonds in the surfaces α-Ag_2WO_4 were calculated as

$$D_b = N_b/A, \hspace{4cm} \text{Eq. 1}$$

where N_b is the number of broken bonds and A is the surface area. The number of broken bonds for each surface was taken from reference [21].

The polyhedron energy band gap energy value for the morphologies of α–Ag_2WO_4 was calculated as follows

$$E_{ap}^{polyhedron} = \sum_i C_i \times E_{gap}^{surf} \hspace{4cm} \text{Eq. 2}$$

where $C_i = A^{surf}/A^{polyedron}$ is the ratio of the surface area (A^{surf}) to the total surface area of the polyhedron ($A^{polyedron}$) and E_{gap}^{surf} is the energy value of the corresponding surface.

3. RESULTS AND DISCUSSION

3.1. Morphology

α–Ag_2WO_4 samples obtained by the CP method using 70% of water and 30% of ethanol, followed by treatment with MAH and exposure to EI and FI irradiations, were investigated by FE-SEM, as shown in **Figure S1** and **Figure 2**. Through the CP method,

168   only hexagonal rod-like morphologies were observed, with preferential growth on the y-

169   axis in the (010) direction (**Figure S1**). These characteristics were previously studied by

170   our research group and are reported in reference [48]. In this method, the clusters of silver

171   and tungsten ions solvated with water and ethanol interact randomly in a polarization

172   process of complex clusters, depending on the moment of the permanent dipole of the

173   neighboring clusters. This short-range interaction induces the first links between the

174   crystal symmetry and its order/disorder. Then, to increase the symmetry and order of the

175   crystal, there is a correlation between the rotation motions of permanent moments in the

176   different complex clusters of silver and tungstate to form the different surfaces.

177

178   **Figure 2.**

179

180   Theoretical calculations reported in the literature show that the morphological

181   shapes of α–Ag_2WO_4 are formed by the combination of the (010), (100), (001), (110),

182   (101), and (011) surfaces [21,48]. Although the theoretical results establish an ideal

183   parallelepiped-like morphology for α–Ag_2WO_4, characterized by the presence of (010),

184   (100), and (001) surfaces with predominant contributions of the (010) and (100) surfaces

185   and a minor proportion of the (001) surface, experimentally a hexagonal rod-like

186   morphology was observed (**Figure S1**). **Table 1** presents the values of E_{surf} according

187   to R. A. Roca and et al. [48], as well as the surface band gap energy (E_{gap}^{surf}) and the

188   percentage of contribution ($\%C_i$) for each morphology of α–Ag_2WO_4.

189   The experimental rod-like morphology of α–Ag_2WO_4 for the CP sample

190   composed of the (010), (100), and (101) surfaces were obtained by destabilizing the E_{suf}

191   of the (010), (110), and (100) surfaces from 0.20 to 1.44 Jm^{-2}, 0.65 to 1.50 Jm^{-2} and

0.38 to 0.70 Jm^{-2}, respectively, as well as by stabilizing the (101) and (001) surfaces

from 0.68 to 0.23 Jm^{-2} and 0.53 to 0.22 Jm^{-2}, respectively (see **Figure 3**).

Figure 3.

In the MAH system, the monitoring of the experiment illustrated the time

dependence in relation to the morphological evolution of α–Ag$_2$WO$_4$ (**Figures 2a-e**).

Morphologies composed of cube-like (highlighted in orange) and rod-like (indicated in

blue) were observed in the samples treated with MAH at 2, 4, 8, and 16 min.

Theoretically, the cube-like morphology composed of the (010), (100), and (001) surfaces

can be obtained by stabilizing the (100) and (001) surfaces (**Figure 3**).

At 32 min of treatment with MAH, a process of redissolution and stabilization of

the (101) surface occurred, with concomitant destabilization of the (100) surface. This

information allows us to understand how the time variation of the MAH treatment in an

alcoholic environment influences particle growth. The microwave radiation induces a

structural disorder through the modification of the bond distance, consequently altering

the internal rotation barrier and vibration of molecules. In turn, the stabilization of

previously unstable surfaces results in a new morphology [7,9]. Thus, at the highest

synthesis time (32 min) the MAH-32 sample (**Figure 2e**) presented no cubes – only rods

behaving similarly to those obtained in the CP sample (**Figure S1**). It is then believed

that at a longer exposure time to microwave irradiation, the cube-like morphology is

rearranged to a rod-like morphology.

Table 1. Calculated density broken bond (nm^{-2}), surface energy (E_{surf}, Jm^{-2}), surface

band gap (E_{gap}^{surf}, eV), percentage of contribution of each surface in the total area (% C_i)

and polyhedron band gap energy for the morphologies of α–Ag$_2$WO$_4$.

Morphology	Surface	D_B	E_{surf}	% C_i	E_{gap}^{surf}	$E_{gap}^{polyhedron}$
Ideal $\alpha - Ag_2WO_4$	(010)	4.68	0.20	52.5	1.39	
	(100)	5.83	0.38	27.6	0.48	0.99
	(001)	6.04	0.53	19.8	0.65	
Rod-like $\alpha - Ag_2WO_4$	(010)	--	1.44	7.3	1.39	
	(001)	--	0.22	13.2	0.65	1.10
	(101)	8.75	0.23	79.4	1.15	
Cube-like $\alpha - Ag_2WO_4$	(010)	--	0.20	42.9	1.39	
	(100)	--	0.30	28.6	0.48	0.92
	(001)	--	0.30	28.6	0.65	

It can be inferred that the microwave treatment directly interferes with the crystal morphology by either totally or partially dissolving the rod-liked crystals or altering the internal rotation movements between the clusters. Thus, in the MAH method, the cube-like morphology is formed by the less energetic surfaces, i.e., (100) and (001), with a decrease in disorder and an increase in symmetry (**Figure 3**). The same behavior was observed in reference [28], in which the MAH method is employed to synthetize α–Ag$_2$WO$_4$ and different morphologies were obtained: hexagonal rod-like elongated, cubic-like, and triangular-like shapes.

Under electron beam irradiation, these morphologies change to a unique rod-like morphology (EI samples indicated by green color in **Figures 2f-j**), whereas under femtosecond laser irradiation they change to the mixed rod- (violet color) and sphere-like morphologies (yellow color) (FI samples in **Figures 2k-o**). The n-type semiconductor, α–Ag$_2$WO$_4$, when irradiated with electrons, grows on its surface metallic silver nanowires [10,11,30], thus forming silver vacancies inside the particle and causing a variation in the

surface energies of the crystalline structure. Therefore, the value of the (101) surface drops from 0.68 to 0.23 Jm^{-2} (**Figure 3**), becoming less energetic, while that of the (100) surface jumps from 0.38 to 0.70 Jm^{-2}, thus becoming more energetic. Even when varying the synthesis times, all samples exhibit agglomerated nature with characteristics similar to those observed in the CP sample (**Figure S1**). In this micrograph, it can also be observed that the hexagonal rod-like morphology is better defined, with few imperfections. This fact can be considered an indication of the effect of electron beam irradiation on the morphology of α–Ag_2WO_4.

Under EI, the energy of the electron beam is transferred to the sample, causing different phenomena, such as atomic position change, surface distortions, electrostatic charge, and local heating in the crystals. Depending on the voltage and the type of sample electron beam will penetrate a few micrometers or nanometers deep into the sample. In our case, the voltage is 30 keV, whose penetration is in the order of nanometers, causing surface defects and atomic mobility that culminate in the formation of Ag nanoparticles on the surface of α-Ag_2WO_4 [11,49]. On the other hand, when a FI is applied, photons are absorbed by the sample to provoke an excitation in the crystal system. To return to the ground state, the system segregates electrons, atoms, and ions from its structure, forming a plasma plume ablation, which is highly energetic. This plume interacts with the irradiated region, promoting energy exchanges, increasing temperature and pressure, accelerating the speed of movement of the species, and ejecting particles. After this highly energetic ablation process, the surface cools very quickly, which modify the surface structure of the material [37,50].

Regarding the morphology obtained by the FI technique (**Figures 2k-o**), it is possible to observe in α–Ag_2WO_4 spherical particles with well-defined edges and irregular extensions, in addition to elongated and slightly curved rods. According to the

elementary mapping performed on the FI-8 sample (**Figure 4**), both the spheres and the rods are composed of the same proportion of Ag, O, and W atoms, thus confirming the change in particle morphology composed of the same α–Ag_2WO_4 polymorph.

Figure 4.

The application of the FI technique leads to the formation of a spherical morphology of α–Ag_2WO_4 powders due to when the femtosecond laser beam interacts with the α-Ag_2WO_4, a nonlinear and multiphoton ionization process occurs, which results in the formation of a plasma plume above the irradiated zone [31,51]. The highly energetic ablation process provokes the breaking of the bonds between the W-O andAg-O, atoms. Further, since the plasma itself can reach temperature and pressure values of up to 1000 K and 10^{12} Pa, respectively [51], such extreme conditions can trigger the sintering of the material that reminds in contact with the plasma Since the plasma plume, which reaches values up to 1000 K, has a lifetime in the region of the ns [52], the plasma can transfer heat to the material surrounding the irradiation zone. Thus, the material that did not undergo sintering just experienced a melting process, resulting in the curvature of its edges. This effect is considered to favor the coalescence of the previously observed rods and cubes, giving rise to the morphology of the spheres.

The analysis in **Figure 2** suggests that in addition to the morphological changes already discussed, another relevant aspect is observed: the presence of silver nanoparticles on the surface of samples as a result of electron beam and femtosecond laser irradiations. This phenomenon has already been well discussed by our group [10,11,24,31,38–40]. These changes in sample morphologies allow us to understand how the surface structure can affect and modify the PL property of a semiconductor.

3.2. Unit cell and lattice parameters

The result of Rietveld refinement (**Table S1**) reveals that the lattice parameters and bond angle of all samples correspond to an orthorhombic structure and *Pn2n* spatial group, which is in agreement with the crystallographic information file in ICSD 4165 card [53]. Moreover, the R_{Bragg} and chi^2 fitting parameters evidence the accordance between the calculated data and the observed XRD patterns. The Rietveld refinement data show the effect of irradiation on the parameters of the unit cell, which were found to change. In general, when all MAH samples are irradiated by EI and FI, there is an expansion in the cell volume, consequently altering the lattice of the samples.

Figure 5 brings a comparison among the geometries for optimized (*opt*–α-AWO), neutral (CP), and irradiated structures (MAH-8, EI-8, and FI-8). From this figure, it is possible to observe variations of the relative positions of the Ag, O, and W atoms on several different constituents $[WO_6]/[AgO_y]$ clusters (y = 7, 6, 4, and 2) of α–Ag_2WO_4. Since the $[AgO_2]$ and $[AgO_4]$ clusters are found in the shell of the unit cell, changes are expected as a result of the strong interaction caused by irradiation, leading to nucleation and formation of metallic Ag [24,54]. Thus, the comparison between the *opt*–α-AWO geometries and MAH-8 structures for the sample treated with MAH indicates variations in the Ag–O distances and O–Ag–O angles, mainly in the $[AgO_2]$ and $[AgO_4]$ clusters. In the $[AgO_2]$ cluster, Ag–O increases from 2.246 to 2.461 Å, while O–Ag–O decreases from 174.42 to 145.05 °. In the case of the Ag–O bond in $[AgO_4]$ clusters, an increase in two bond distances is observed. When the MAH-8 sample is exposed to EI, both Ag–O distance and O–Ag–O angle in the $[AgO_2]$ cluster remain almost unchanged, going from 2.461 to 2.455 Å and from 145.05 to 147.42 °, respectively, whereas the Ag–O distance in the $[AgO_4]$ clusters undergoes increases. On the other hand, when a femtosecond laser

307 is applied, the Ag–O distance in the [AgO$_2$] cluster decreases from 2.461 to 2.193 Å,

308 while the O–Ag–O angle increases from 145.05 to 170.42 º. Regarding the [AgO$_4$]

309 clusters, it is possible to note a shortening average of the Ag–O distance. With respect to

310 the different types of [WO$_6$] clusters, in all cases, the W–O bond distances of the

311 irradiated samples undergo variations corresponding to W1, in which an average

312 lengthening is observed.

313   A careful analysis of the Ag–O and W–O bond distances for all samples were

314 performed, and the observed values are listed in **Table S2**.

315   From **Figure 5** and the values in **Table S2**, we can infer that the MAH treatment

316 induces a larger structural organization in the α–Ag$_2$WO$_4$, which is evidenced through the

317 average lengthening of the Ag–O and W–O bonds in the [WO$_6$]/[AgO$_y$] clusters (y = 7,

318 6, 4, and 2). Considering the EI, it can be noted that the irradiation with electrons leads

319 to structural changes in the [AgO$_4$] and [W1O$_6$] clusters. On the other hand, FI induces

320 an average shortening of Ag–O and an average lengthening of W1–O bond distances in

321 the clusters of α–Ag$_2$WO$_4$ when compared with both MAH samples and the optimized

322 system. These results explain the constant changes in the crystal lattice and the size

323 reduction of [AgO$_y$] clusters proposed by our group [22], which may also be induced by

324 rod-to-sphere morphology changes in the irradiated samples.

325

326   **Figure 5.**

327

328   To investigate the effect of irradiation on the particle surface, XPS measurements

329 were conducted. Such analyses were performed in the samples that had their morphology

330 and the PL property changed, that is, MAH-8, EI-8, and FI-8.

Figure 6 shows the high-resolution spectra of O $1s$, which were fitted with three components. The strong peak around 530.03 eV, 529.83 eV, and 530.07 eV for the MAH-8, EI-8, and FI-8 samples, respectively, are attributed to the O atom in the α-Ag_2WO_4 lattice. The peak at 531.43 eV, 531.54 eV, and 531.92 eV, respectively, are assigned to oxygen defects in the lattice, such as oxygen vacancies (V_O) [55]. Lastly, the peak in the high binding energy, i.e., above 533 eV, is related to adsorbed oxygen on the surface [55,56].

Changes in the profile of the high-resolution spectrum of O $1s$ indicate a high percentage of adsorbed oxygen on the surface of the EI-8 and FI-8 samples in comparison with MAH-8. Additionally, there is a decrease in the area percentage of the lattice oxygen to 69.97% for MAH-8, 48.00% for EI-8, and 37.66% for FI-8, as well as an increase in the area percentage ascribed to defect oxygen to 20.98%, 27.88% and 38.10% for the MAH, EI and FI samples, respectively. This indicates a possible formation of oxygen vacancies in the EI and FI samples. The vacancies formed are a charge compensation due to destabilization of the (010) surface along the transformation of morphology from cubes-like into rods-like.

Furthermore, surfaces can be stabilized by reducing surface charge density via different mechanisms: creating surface states, redistributing charge between atoms, removing atoms, adding charged impurities to the surface, or creating faces [57,58]. In the process of electron beam irradiation and femtosecond laser irradiations, we observed the destabilization of the surface (010), by the conversion of cubic particles into rods, which was compensated by the removal of surface oxygen atoms and by chemoadsorption of species (O^- and O^{2-}) on the surface, according to the XPS results.

The increment in oxygen vacancies and impurities, via FI, may be related to the fact that the experiment is carried out in an environment, which allows the exchange of

charges and specie. It is known that the greater exposure of a given crystalline surface influences the properties of materials [59]. An analyis of the theoretical results renders that the (010) surfacepresent the highest value of surface energy in the rod morphology. Extrapolating this data to literature [59], we suppose that to compensate the energetic instability, superficial oxygen vacancies were created.

Figure S2a shows that the Ag *3d* spectra were better fitted using one component. The high-intensity peaks located at approximately 368 eV and 374 eV are related to the $3d_{5/2}$ and $3d_{3/2}$ orbitals, respectively, with Ag^+ binding energy. No significant changes were observed among the spectra of the samples.

The XPS technique also provided information on the chemical environment of the W element, which is considered to be the lattice-forming atom. **Figure S2b** displays the XPS spectra of the W *4f* for the MAH-8, EI-8, and FI-8 samples. The binding energy corresponds to the $4f_{7/2}$ and $4f_{5/2}$ orbitals of W^{6+} in the α–Ag_2WO_4 lattice [4,60,61]. The XPS spectra reveal a similar profile in all samples, with no changes in the oxidation state or chemical environment of the structural W atom, nor even for the EI and FI samples. Therefore, it can be concluded that the irradiation process changes the environment around oxygen atoms due to the formation of metallic Ag and V_O vacancies, consequently leading to distortions in the angle and bond distance of the Ag and W clusters (**Table S2**).

Figure 6.

3.3. Structural characterization

Figure S3 displays the Raman spectra in the range of 60-960 cm^{-1} at room temperature. According to Turkovič et al. (1977) [62], there are 21 known Raman modes for α-Ag_2WO_4 ($6A_{1g}$, $5A_{2g}$, $5B_{1g,}$ and $5B_{2g}$). As it can be observed in **Figures S3a-d**, six

381 Raman modes were detected for all samples ($1A_{1g}$, $1A_{2g}$, $3B_{1g}$, and $1B_{2g}$); the remaining

382 modes were not detectable experimentally because of their low intensities. External

383 vibrational modes of interaction between silver and tungstate ion and $[AgO_y]$ ($y = 7, 6, 4$,

384 2) clusters can be identified between 100 and 500 cm^{-1}, whereas internal vibrational

385 modes assigned to the vibrations in the $[WO_6]$ clusters can be detected between 500 and

386 1000 cm^{-1} [28,34,63]. It is possible to observe in both materials two intense bands: one at

387 102 cm^{-1}, attributed to the stretching of T'(Ag^+/W^{6+}) binding [64], and another at 877 cm^{-1}

388 , assigned to the symmetrical stretching of the W–O bond in the octahedral $[WO_6]$ cluster

389 [28].

390 The comparison between the relative experimental and theoretical positions of

391 these vibrational modes is illustrated in **Figure S3e** and summarized in **Table S3**,

392 confirming the good agreement between the experimental and theoretical modes.

393 Following the Raman discussion on the short-range structural disorder, XANES

394 allowed us to visualize a local disorder, which in our case was around the tungsten atom.

395 In the past decade, our research group has employed the XANES technique to study the

396 local structure of various semiconducting metal oxides, such as tungstates, titanates, and

397 vanadates among others [19,65–69].

398 Herein, we performed XANES measurements to investigate the effect of

399 irradiation on the local structure around W atoms. **Figure S4a** displays the W-L1 XANES

400 spectra of the as-prepared CP sample and some standards used as reference samples

401 (Na_2WO_4, WO_2, and monoclinic WO_3). In **Figure S4a**, it is possible to observe a

402 pronounced peak (here denoted as P1) in the Na_2WO_4 spectrum, more specifically in the

403 pre-edge region, as well as a shoulder in the m-WO_3 standard and the CP sample spectra.

404 The physical origin of such electronic transition (peak P1) is described elsewhere

405 [19,70,71].

It is well established that an intense pre-peak in the W-L1 edge XANES spectrum has been found in materials constituted by tetrahedral units (WO_4), such as the Na_2WO_4 compound [5,71]. The electronic transition responsible for P1 pre-peak is forbidden in the materials that exhibit regular $[WO_6]$ units. However, compounds presenting non-regular octahedral symmetry (distorted WO_6 clusters) have been found to present a less intense pre-peak similar to that in the WO_3 spectrum [70,71]. From the analysis of the spectrum of the CP sample, it is possible to observe its similarity with the WO_3 standard spectrum. It is then plausible to affirm the presence of distorted $[WO_6]$ clusters in the as-prepared CP sample. Furthermore, by comparing the spectra of the α–Ag_2WO_4 samples (**Figure S4b**) it is evident the similarity with the XANES spectra (both in the pre- and post-edge regions). Such behavior reveals that the microwave-assisted hydrothermal treatment, as well as the irradiation processes (EI and FI), resulted in samples constituted by distorted octahedral WO_6 clusters.

3.4. Density of states

The experimental optical band gap was estimated using the Wood-Tauc relation [72,73] and the Kubelka-Munk equation [59,60], evidencing a slight variation from 3.09 to 3.32 eV (**Figure S5**) for the MAH, EI, and FI samples. The experimental results show that when the CP sample is submiiited to MAH treatment for 2 minutes, the band gap value decreases from 3.13 eV to 3.08 eV. In contrast, for the MAH-4, MAH-8, MAH-16, and MAH-32 samples, the band gap increases. Later, when these samples are under EI, is observed that except for the EI-2 sample, the band gap decrease in all cases. For the FI-2 and FI-4 samples present an increase in the band gap, while for the FI-8, FI-16, and FI-32 samples, an opposite effect can be sensed. Structural order-disorder effects induced by

the radiation as well as the morphology, time process and shape powder can explain the band gap decrease/increase of α-Ag_2WO_4.

The electronic structure of α-Ag_2WO_4 was analyzed from the partial density of states (PDOS) of the *4d*, *5d,* and *2p* orbitals of Ag, W, and O atoms, respectively (**Figure 7),** where the valence band maximum (VBM) is set to zero. In terms of contributing states, the representation is similar for all samples, according to the composition of the valence band (VB) and conduction band (CB) of the different samples. As already known, for α–Ag_2WO_4 the VB is formed by the hybridization of *4d$_{xy}$* and O *2p$_z$* orbitals, whereas the bottom of the CB is mainly composed of W *5d* orbitals, more specifically *5d$_z^2$* orbitals. However, differences in topology occur among the PDOS of neutral and irradiated samples. In the PDOS of the neutral sample, there is discontinuation in the VB, leading to two distinct Ag *4d* blocks. Such characteristic is maintained in the EI-8 sample, while in the PDOS of the MAH-8 and FI-8 samples the double-peak structure disappears.

Figure 7.

In the MAH-8 and FI-8 samples (**Figure 7c**), localized states of the O *2p$_x$*, *2p$_y$* and *2p$_z$* and Ag *4d$_{xy}$* orbitals are evidenced in the Fermi region, as well as localized *5d$_x^2$-$_y^2$* and *5d$_z^2$* orbitals forming the bottom of the CB in these samples. The localized density of *2p* and W *5d* states situated at the Fermi level and the bottom of the CB, respectively, favors the electronic transfer from the O *2p* to W *5d* states, which are necessary for the excitation process of the tungstate groups. These observations in the electronic properties of the different samples are associated with the structural disorder induced by the irradiation in the α–Ag_2WO_4 lattice, as seen in **Figure 5**.

Figure 8 shows the PL spectra of α–Ag$_2$WO$_4$ samples measured at room temperature and excited at 355 nm. The PL spectra encompass the whole visible region and part of the near-infrared region, presenting a broadband profile. The small changes in the profile of the PL spectrum between the same group are related to different degrees of order/disorder in the O–Ag and O–W bond lengths. Therefore, by analyzing the PL spectra we can understand how the MAH treatment time, and electron beam and femtosecond laser irradiations affect the emission spectrum of α–Ag$_2$WO$_4$.

Figure 8.

The CP and EI samples with rod-like morphology (**Figure S2** and **Figure 2f-j**) have two maximum emission centers: around the green (550 nm) and the red (733 nm) regions (**Figure 8a,b**). The FI sample with rod- and sphere-like morphologies presented the same emission centers (**Figure 2k-o** and **Figure 8c**). When the sample is submitted to MAH at synthesis times between 2 and 16 min, two types of morphologies are observed (rod- and cube-like, **Figures 2a-d**), and the maximum emission center around 550 nm is favored (**Figure 8a**). However, the sample treated with MAH at a prolonged synthesis time of 32 min, in addition to only hexagonal rod-like particle morphology, presents two maximum emission centers similar to those of the CP sample.

It is well known that the PL property of α–Ag$_2$WO$_4$ is strongly correlated by photogenerated electron-hole pair processes and in terms of the electronic transition between the VB (*2p* levels of oxygen atoms and *4d* level of silver atoms) and the CB (*5d* levels of tungsten atoms) as well as the contribution of intermediate levels between the VB and CB [22,32,33,67,75].

478   The blue band is attributed to the radiative transition from the O_{2p} states to the

479   W_{5d} states while the green band is due to the electronic transition from the $Ag^+–V_O$ defects

480   level to the VB [63]. Blue/Green emission was also related to distorted $[WO_6]$ octahedral,

481   while red emission to the $[AgO_y]$ (y = 2, 4, 6, and 7) clusters that form complex vacancies,

482   inducing more disorder and deeper defects in the forbidden band gap [32,39].

483   Furthermore, the $[AgO_y]$ (y = 2, 4, 6, and 7) and $[WO_6]$ clusters in pairs have

484   extrinsic defects, which are linked to order-disorder effects in the electronic structure,

485   surface, and interfaces, which create additional energy states above the VB and below the

486   CB, which decrease the band gap [32,67]. However, a specific assignment of surface and

487   the clusters that are present on each surface that contributes to PL emission has not been

488   observed. Here, we can observe the influence of particle morphology and surface band

489   gap since the distortions in the lattice favor different distributions of electronic state in

490   the surface (**Figure 9**).

491

492   **Figure 9.**

493

494   To analyze the difference between the emission spectrum and the contribution of

495   each surface (**Figure 9**), a comparison among the MAH-8, EI-8, and FI-8 samples with

496   the cube-, rod- and sphere-like morphologies, respectively, is presented in **Figure 10**.

497   Since each of the surfaces of $α–Ag_2WO_4$ presents a different band gap energy (E_{gap}^{surf})

498   value, it is expected that each surface has a specific contribution in the PL property. This

499   can be justified by the fact that each surface is quite different in terms of the coordination

500   number of atoms, the distance between adjacent atoms, and available electron density

501   [22,30].

502

Figure 10.

504

505   The theoretical E_{gap} values of surfaces and the rod- and cube-like morphologies

506   of α–Ag₂WO₄ are listed in **Table 1.** According to the results, all surfaces studied show

507   E_{gap}^{surf} values reduced in comparison to the E_{gap} value of the bulk. The density of defects

508   on the surface can justify the existence of intermediary states in the band region of the

509   bulk, which come from the number of Ag−O and W−O bonds that are broken when a

510   slab surface is created. To quantify the defects on the surface, the density of broken bonds

511   was calculated as $D_b = N_b/A$, there N_b is the number of broken bonds and A is the surface

512   area. The results corroborate that those surfaces with higher D_b values present the lowest

513   band gap (**Table 1)** and consequently, intermediary states (**Figure 9**).

514   Regarding the $E_{gap}^{polyhedron}$ for each experimental morphology, the results reveal

515   that in passing from ideal to the experimental rod-like morphology, the $E_{gap}^{polyhedron}$ value

516   increase from 0.99 eV to 1.10 eV due to the appearance of the (101) surface which comes

517   to dominate the Wulff construction (79.4 %) for the rod-like morphology and has a band

518   gap of 1.15 eV. The (010) and (001) surfaces are also exposed in this morphology in a

519   lower proportion (7.3 % and 13.2%, respectively). In the case of the passing from ideal

520   to the experimental cube-like morphology, the $E_{gap}^{polyhedron}$ decrease from 0.99 eV to 0.92

521   eV at the time that (001) and (100) surfaces that have the lower band gap values 0.65 eV

522   and 0.48 eV, respectively, increase their contribution (28.6 % each one) to the cube-like

523   morphology that exposed the (010) surface (42.9 %) which have band gap (1.39 eV).

524   It is worth nothing that theoretical values of band gap energy are not the same that

525   those obtained experimentally because the experimental techniques used for such

526   measurements considering the effect bulk/surface of the material and in the calculations

527   have been considered only the exposed surface structures at the morphology.

Figure 10a shows that both CP and EI-8 samples are composed only of rod-like morphologies. The PL spectrum for the CP and EI-8 samples showed two maximum emission centers – around 550 nm and 733 nm – regions. In the case of the MAH-8 sample, it is composed of both cube- and rod-like morphologies and although the PL spectrum also present two emission centers, is observed that the maximum emission center around 550 nm is favored while the emission center is 733 nm present intensity lower. Finally, the sample irradiated by femtosecond laser (FI-8) with rod- and sphere-like morphologies presented an equilibrium in the maximum emission centers with a slight shift to the red region. Based on these results, we can conclude that (010) and (101) surfaces contribute to the emission centers at 550 nm and 733 nm, respectively.

As previously mentioned, (010) surface has the highest band gap, therefore it tends to contribute to the highest energies emission (**Figure 10b**), in addition, is present in both morphologies, see **Table 1,** and is the aim component of the cube-like morphology, thus, the presence of both cube and rod-like morphologies in the sample contributed to the emission to 550 nm. In contrast, (101) surface is the main component of the rod-like morphology, and therefore the sample only with rod shows a defined emission at 733 nm. The highest intensity of emission in 550 nm is associated with the presence of localized states in the forbidden band gap due to (010) surface, see **Figure 9** and **Figure 10b**, which favored the probability of the transition in this surface.

As has been established in the (101) surface are present distorted $[WO_6]_d$ cluster, and the undercoordinate $[AgO_5 \cdot 2V_O^x]$, $[AgO_4 \cdot 3V_O^x]$, and $[WO_5 \cdot V_O^x]$ clusters. The complete distorted $[WO_6]_d$ clusters are considered as a source of electrons due to while the undercoordinate $[AgO_5 \cdot 2V_O^x]$, $[AgO_4 \cdot 3V_O^x]$ clusters, and $[WO_5 \cdot V_O^x]$ clusters supporting charge positive are considered a source of the hole [76,77].

In the case of the (010) surface complete distorted $[WO_6]_d$ and $[AgO_4]_d$ clusters present in the surface are a source of electrons while undercoordinate $[AgO_5 \cdot 2V_O^x]$ clusters are a source of holes, thus, the transfer electron-hole occur from complete distorted clusters to undercoordinate $[AgO_5 \cdot 2V_O^x]$ clusters, the above also explain the contribution of the (010) surface to the PL property [21].

Moreover, the cube- and rod-like morphologies have a stable (001) surface, which has the E_{gap}^{surf} (0.65 eV), see **Table 1** and **Figure 10b**. The (001) surface has a percentage of total area contribution in both morphologies of 28.6% and 13.2%, respectively. The (001) surface has [WO$_5$.V_O^x], [AgO$_5$.$2V_O^x$], [AgO$_4$.$3V_O^x$], and [AgO$_4$.$2V_O^x$] clusters [21]. The cube-like morphology also has a stable (100) surface, which has the lowest E_{gap}^{surf} (0.48 eV), **Figure 10b**. The (100) surface has [WO$_5$.$2V_O^x$], and two [AgO$_5$.$2V_O^x$] clusters [21].

In general, the samples with cube-like morphologies showed a maximum center emission in the green region, while those with particles with only rod-like morphology showed two maximum emission centers (in the green and red regions). Differently, the sphere-like morphology presented an equilibrium in the emission centers. The PL behavior demonstrates the influence of many factors, such as the orientation between particles, the variations in the particles size distribution, the morphology of the particles, and surface defects [32].

The XYZ color space created by the International Commission on Illumination (abbreviated as CIE) serves as a standa.rd reference to represent the color emitted by the materials, and this color is expressed by a resulting chromaticity symbolized by the coordinates (x, y) [61]. The chromaticity coordinates x and y under excitation of 355 nm were obtained in the CIE XYZ color space (**Figure S6**), and the detailed information is shown in **Table S4**.

577   The MAH group revealed variation in their color from orange to red (**Figure S6a**)

578   due to the synthesis time, which disorganized the [AgO$_y$] clusters. The CIE diagram of

579   the EI and FI groups also showed a color variation from orange to red (**Figure S6b**).

580   Among the samples submitted to femtosecond laser irradiation, the FI-32 was found to

581   be the most resistant to the laser action, remaining practically unchanged when compared

582   to the MAH-32 (**Figure S6c** and **Table S4**). The other samples migrated from orange to

583   red, following what was observed for samples irradiated by electrons. Therefore, the PL

584   measurements demonstrated that microwave, electron beam, and femtosecond laser

585   irradiations altered the electronic density of the bulk and surface since the behavior of the

586   samples changed after irradiation. However, the sample obtained at the longest synthesis

587   time did not show variation in the density of V_{Ag} and V_O vacancies when subjected to

588   electron or femtosecond irradiation, which is possibly related to its more stable rod-like

589   morphology.

590

591   **4. CONCLUSION**

592   In summary, in this work, we discussed the influence of morphology, surface band

593   gap, and microstructure on the PL property of α–Ag$_2$WO$_4$ samples obtained by the CP

594   method, followed by treatment with MAH at different synthesis times and two different

595   irradiation processes: electron beam and femtosecond laser. The experimental and

596   theoretical study clarifies the important relationship between the DOS of different

597   surfaces and the PL property. It was observed that the use of different ways of treating

598   the samples successfully changed the surface characteristics, microstructure, and

599   electronic density of the α–Ag$_2$WO$_4$ materials. Electron beam and femtosecond laser

600   irradiations were found to cause expansion of the unit cell, form oxygen vacancies on the

601   surface, change the angle and distance between O–Ag and O–W bonds, and modify the

particle morphology to rod-, cube- and sphere-like. The theoretical calculations showed how changes in the microstructure, morphology, and surface band gap values can alter the distribution of electron density, and consequently the emission centers. Cube-like morphology shows a high contribution of the (010) surface, while rod-like morphologies showed the contribution of (010) surface and (101) surface. Moreover, the sample submitted to a longer synthesis time of 32 min in the microwave system presented the most stable rod-like morphology and high resistance to the disorder of the network-modifying $[AgO_y]$ clusters. Therefore, the more ordered the network-forming $[WO_6]$ clusters, the more difficult it will be to introduce defects. For this reason, no significant changes were observed in the PL property. These results enrich the literature regarding the effect of different techniques associated with microstructure, morphology, and band gap energies on the PL properties of semiconductor materials.

ACKNOWLEDGMENTS

627 **AUTHOR INFORMATION**

628 **Corresponding Authors:**

629 elson.liec@gmail.com

630 mayaramondego.ufma@gmail.com

631 anacmora@gmail.com

632

633 **ORCID**

634 Mayara Mondego Teixeira: 0000-0001-9038-0024

635 Lilian Cruz Santos: 0000-0001-5395-5650

636 Ana Cristina Mora Tello: 0000-0003-4168-5774

637 Priscila Barros de Almeida: 0000-0003-4983-2695

638 Jussara Soares da Silva: 0000-0002-5063-7603

639 Letícia Laier: 0000-0002-6293-9393

640 Lourdes Gracia: 0000-0001-9684-2568

641 Marcio Daldin Teodoro: 0000-0002-3557-5555

642 Luís Fernando da Silva: 0000-0001-6257-5537

643 Juan Andrés: 0000-0003-0232-3957

644 Elson Longo: 0000-0001-8062-7791

645

646 **NOTES**

647 The authors declare no competing financial interest.

648

649 **REFERENCES**

650 [1]   Y. Li, Y. Li, S. Ma, P. Wang, Q. Hou, J. Han, S. Zhan, Efficient water disinfection

651   with Ag_2WO_4-doped mesoporous g-C_3N_4 under visible light, Journal of Hazardous

27

Materials. 338 (2017) 33–46. doi:10.1016/j.jhazmat.2017.05.011.

[2] M. Pirhashemi, A. Habibi-Yangjeh, Preparation of novel nanocomposites by deposition of Ag_2WO_4 and AgI over ZnO particles: Efficient plasmonic visible-light-driven photocatalysts through a cascade mechanism, Ceramics International. 43 (2017) 13447–13460. doi:10.1016/j.ceramint.2017.07.049.

[3] Y. Li, B. Zhu, J. Yu, W. Ho, P. Xia, Fabrication and photocatalytic activity enhanced mechanism of direct Z-scheme $g-C_3N_4/Ag_2WO_4$ photocatalyst, Applied Surface Science. 391 (2016) 175–183. doi:10.1016/j.apsusc.2016.07.104.

[4] H. Li, Y. Zhou, L. Chen, W. Luo, Q. Xu, X. Wang, M. Xiao, Z. Zou, Rational and scalable fabrication of high-quality WO_3/CdS core/shell nanowire arrays for photoanodes toward enhanced charge separation and transport under visible light, Nanoscale. 5 (2013) 11933–11939. doi:10.1039/c3nr03493c.

[5] A. Kuzmin, J. Purans, Local atomic and electronic structure of tungsten ions in AWO_4 crystals of scheelite and wolframite types, Radiation Measurements. 33 (2001) 583–586. doi:10.1016/S1350-4487(01)00063-4.

[6] N.F.A. Neto, P.M. Oliveira, M.R.D. Bomio, F. V Motta, Effect of temperature on the morphology and optical properties of Ag_2WO_4 obtained by the co-precipitation method : Photocatalytic activity, Ceramics International. 45 (2019) 15205–15212. doi:10.1016/j.ceramint.2019.05.006.

[7] H.P. Marques, A.R. Canário, A.M.C. Moutinho, O.M.N.D. Teodoro, Shaping Ag clusters on Titania, Journal of Physics: Conference Series. 61 (2007) 775–779. doi:10.1088/1742-6596/61/1/155.

[8] B. Liu, Z. Hu, Y. Chen, K. Sun, X. Pan, Y. Che, Ultrafast pulsed laser ablation for synthesis of nanocrystals, Nanoengineering: Fabrication, Properties, Optics, and Devices IV. 6645 (2007) 66450R. doi:10.1117/12.736522.

677 [9] K.J.Rao, B.Vaidhyanathan, M.Ganguli, P.A.Ramakrishnan. Synthesis of

678   Inorgannic Solids Using Microwaves. Chem. Mater., 11 (1999) 882–895.

679   doi.org/10.1021/cm9803859

680 [10] M.A. San-Miguel, E.Z. Da Silva, S.M. Zanetti, M. Cilense, M.T. Fabbro, L.

681   Gracia, J. Andrés, E. Longo, In situ growth of Ag nanoparticles on α-Ag_2WO_4

682   under electron irradiation: Probing the physical principles, Nanotechnology. 27

683   (2016). doi:10.1088/0957-4484/27/22/225703.

684 [11] J.C. Sczancoski, S.M. Johnson, S. Pereira, E. Longo, E.R. Leite, Atomic diffusion

685   induced by electron-beam irradiation : An in situ study of Ag structures grown

686   from α-Ag_2WO_4, (2018). doi:10.1021/acs.cgd.8b01076.

687 [12] Y.J. Zhu, F. Chen, Microwave-assisted preparation of inorganic nanostructures in

688   liquid phase, Chemical Reviews. 114 (2014) 6462–6555. doi:10.1021/cr400366s.

689 [13] A. Mirzaei, G. Neri, Microwave-assisted synthesis of metal oxide nanostructures

690   for gas sensing application: A review, Sensors and Actuators, B: Chemical. 237

691   (2016) 749–775. doi:10.1016/j.snb.2016.06.114.

692 [14] S.C. Motshekga, S.K. Pillai, S. Sinha Ray, K. Jalama, R.W.M. Krause, Recent

693   trends in the microwave-assisted synthesis of metal oxide nanoparticles supported

694   on carbon nanotubes and their applications, Journal of Nanomaterials. 2012

695   (2012). doi:10.1155/2012/691503.

696 [15] D. Zhang, Y. Zhang, Y. Fan, N. Luo, Z. Cheng, J. Xu, Micro-spherical $ZnSnO_3$

697   material prepared by microwave-assisted method and its ethanol sensing

698   properties, Chinese Chemical Letters. 31 (2020) 2087–2090.

699   doi:10.1016/j.cclet.2020.01.004.

700 [16] R.E. Newnham, S.J. Jang, M. Xu, F. Jones, This Paper Is a Component Part of the

701   Following Compilation Report : Authored Sections of Proceeding, Annals,

702   Symposia, Etc. However, the Component Should Be Considered Within The

703   Context of the Overall Compilation Report and Fundamental Interaction, Ceramic

704   Transactions. Volume 21. Proceedsing of the Symposium on Microwave Theory

705   and Application in Materials Processing Annual Meetings of the American Cermic

706   Society (23rd). 21 (1991).

707 [17] T. Sin Tee, T. Chun Hui, C. Wu Yi, Y. Chi Chin, A.A. Umar, G. Riski Titian, L.

708   Hock Beng, L. Kok Sing, M. Yahaya, M.M. Salleh, Microwave-assisted hydrolysis

709   preparation of highly crystalline ZnO nanorod array for room temperature

710   photoluminescence-based CO gas sensor, Sensors and Actuators, B: Chemical. 227

711   (2016) 304–312. doi:10.1016/j.snb.2015.12.058.

712 [18] H.W. Kim, Y.J. Kwon, A. Mirzaei, S.Y. Kang, M.S. Choi, J.H. Bang, S.S. Kim,

713   Synthesis of zinc oxide semiconductors-graphene nanocomposites by microwave

714   irradiation for application to gas sensors, Sensors and Actuators, B: Chemical. 249

715   (2017) 590–601. doi:10.1016/j.snb.2017.03.149.

716 [19] L. Cruz, M.M. Teixeira, V. Teodoro, N. Jacomaci, L.O. Laier, M. Assis, N.G.

717   Macedo, A.C.M. Tello, L.F. da Silva, G.E. Marques, M.A. Zaghete, M.D. Teodoro,

718   E. Longo, Multi-dimensional architecture of Ag/α-Ag$_2$WO$_4$ crystals: insights into

719   microstructural,   morphological,   and   photoluminescence   properties,

720   CrystEngComm. 22 (2020) 7903–7917. doi:10.1039/d0ce00876a.

721 [20] L.O. Laier, M. Assis, C.C. Foggi, A.F. Gouveia, C.E. Vergani, L.C.L. Santana,

722   L.S. Cavalcante, J. Andrés, E. Longo, Surface-dependent properties of α-Ag$_2$WO$_4$:

723   a joint experimental and theoretical investigation, Theoretical Chemistry

724   Accounts. 139 (2020) 1–11. doi:10.1007/s00214-020-02613-z.

725 [21] N.G. Macedo, A.F. Gouveia, R.A. Roca, M. Assis, L. Gracia, J. Andrés, E.R. Leite,

726   E. Longo, Surfactant-Mediated Morphology and Photocatalytic Activity of α-

727   Ag$_2$WO$_4$ Material, Journal of Physical Chemistry C. 122 (2018) 8667–8679.

728   doi:10.1021/acs.jpcc.8b01898.

729 [22] M. Assis, R.A. Pontes Ribeiro, M.H. Carvalho, M.M. Teixeira, Y.G. Gobato, G.A.

730   Prando, C.R. Mendonça, L. De Boni, A.J. Aparecido De Oliveira, J. Bettini, J.

731   Andrés, E. Longo, Unconventional Magnetization Generated from Electron Beam

732   and Femtosecond Irradiation on α-Ag$_2$WO$_4$: A Quantum Chemical Investigation,

733   ACS Omega. 5 (2020) 10052–10067. doi:10.1021/acsomega.0c00542.

734 [23] E. Longo, W. Avansi, J. Bettini, J. Andrés, L. Gracia, In situ Transmission Electron

735   Microscopy observation of Ag nanocrystal evolution by surfactant free electron-

736   driven synthesis, Scientific Reports. 6 (2016) 1–8. doi:10.1038/srep21498.

737 [24] E. Longo, L.S. Cavalcante, D.P. Volanti, A.F. Gouveia, V.M. Longo, J.A. Varela,

738   M.O. Orlandi, J. Andrés, Direct in situ observation of the electron-driven synthesis

739   of Ag filaments on α-Ag$_2$WO$_4$ crystals, Scientific Reports. 3 (2013) 4–7.

740   doi:10.1038/srep01676.

741 [25] J. Andrés, L. Gracia, P. Gonzalez-Navarrete, V.M. Longo, W. Avansi, D.P.

742   Volanti, M.M. Ferrer, P.S. Lemos, F.A. La Porta, A.C. Hernandes, E. Longo,

743   Structural and electronic analysis of the atomic scale nucleation of Ag on α-

744   Ag$_2$WO$_4$ induced by electron irradiation, Scientific Reports. 4 (2014) 1–7.

745   doi:10.1038/srep05391.

746 [26] W. da S. Pereira, J. Andrés, L. Gracia, M.A. San-Miguel, E.Z. da Silva, E. Longo,

747   V.M. Longo, Elucidating the real-time Ag nanoparticle growth on α-Ag$_2$WO$_4$

748   during electron beam irradiation: experimental evidence and theoretical insights ,

749   Physical Chemistry Chemical Physics. 17 (2015) 5352–5359.

750   doi:10.1039/c4cp05849f.

751 [27] J. Andrés, A.F. Gouveia, L. Gracia, E. Longo, G. Manzeppi Faccin, E.Z. da Silva,

752   D.H. Pereira, M.A. San-Miguel, Formation of Ag nanoparticles under electron

753   beam irradiation: Atomistic origins from first-principles calculations, International

754   Journal of Quantum Chemistry. 118 (2018) 1–15. doi:10.1002/qua.25551.

755   [28] M. Longo, C.C. De Foggi, M.M. Ferrer, A.F. Gouveia, R.S. Andre, W. Avansi,

756   C.E. Vergani, A.L. Machado, J. Andre, A.C. Hernandes, E. Longo, P.O. Box,

757   Potentiated Electron Transference in α-Ag$_2$WO$_4$ Microcrystals with Ag

758   Nanofilaments as Microbial Agent Vale r, (2014). doi:10.1021/jp410564p.

759   [29] M. Assis, E. Cordoncillo, R. Torres-mendieta, H. Beltrán-mir, G. Mínguez-vega,

760   R. Oliveira, E.R. Leite, C.C. Foggi, C.E. Vergani, E. Longo, J. Andrés, Towards

761   the scale-up of the formation of nanoparticles on α-Ag$_2$WO$_4$ with bactericidal

762   properties by femtosecond laser irradiation, (2018) 1–11. doi:10.1038/s41598-

763   018-19270-9.

764   [30] N.G. Macedo, T.R. Machado, R.A. Roca, M. Assis, C.C. Foggi, V. Puerto-Belda,

765   G. Mínguez-Vega, A. Rodrigues, M.A. San-Miguel, E. Cordoncillo, H. Beltrán-

766   Mir, J. Andrés, E. Longo, Tailoring the Bactericidal Activity of Ag

767   Nanoparticles/α-Ag$_2$WO$_4$ Composite Induced by Electron Beam and Femtosecond

768   Laser Irradiation: Integration of Experiment and Computational Modeling, ACS

769   Applied Bio Materials. 2 (2019) 824–837. doi:10.1021/acsabm.8b00673.

770   [31] M. Assis, T. Robeldo, C.C. Foggi, A.M. Kubo, G. Mínguez-Vega, E. Condoncillo,

771   H. Beltran-Mir, R. Torres-Mendieta, J. Andrés, M. Oliva, C.E. Vergani, P.A.

772   Barbugli, E.R. Camargo, R.C. Borra, E. Longo, Ag Nanoparticles/α-Ag$_2$WO$_4$

773   Composite Formed by Electron Beam and Femtosecond Irradiation as Potent

774   Antifungal and Antitumor Agents, Scientific Reports. 9 (2019) 1–15.

775   doi:10.1038/s41598-019-46159-y.

776   [32] E. Longo, D.P. Volanti, V.M. Longo, L. Gracia, I.C. Nogueira, M.A.P. Almdeira,

A.N. Pinheiro, M.M. Ferrer, L.S. Cavalcante, J. Andrés, Toward an understanding of the growth of Ag filaments on α-Ag$_2$WO$_4$ and their photoluminescent properties: A combined experimental and theoretical study, Journal of Physical Chemistry C. 118 (2014) 1229–1239. doi:10.1021/jp408167v.

[33] A. Sreedevi, K.P.Priyanka, K.K.Babitha, S. Ganesh, T. Varghese, Influence of electron beam irradiation on structural and optical properties of α-Ag$_2$WO$_4$ nanoparticles, Micron. 88 (2016) 1–6. doi:10.1016/j.micron.2016.05.003.

[34] Z. Lin, J. Li, Z. Zheng, J. Yan, P. Liu, C. Wang, G. Yang, Electronic Reconstruction of α-Ag$_2$WO$_4$ Nanorods for Visible-Light Photocatalysis, ACS Nano. 9 (2015) 7256–7265. doi:10.1021/acsnano.5b02077.

[35] M. Assis, M.A. Ponce, A.F. Gouveia, D. Souza, J.P. de Campos da Costa, V. Teodoro, Y.G. Gobato, J. Andres, C. Macchi, A. Somoza, E. Longo, Revealing the nature of defects in α-Ag$_2$WO$_4$ by positron annihilation lifetime spectroscopy: A joint experimental and theoretical study, Crystal Growth and Design. 21 (2021) 1093–1102. doi:10.1021/acs.cgd.0c01417.

[36] C.C. dos Santos, M. de Assis, T.R. Machado, P.F. dos Santos Pereira, G. Minguez-Vega, E. Cordoncillo, H. Beltran-Mir, C. Doñate-Buendía, J. Andrés, E. Longo, Proof-of-Concept Studies Directed toward the Formation of Metallic Ag Nanostructures from Ag$_3$PO$_4$ Induced by Electron Beam and Femtosecond Laser, Particle and Particle Systems Characterization. 36 (2019) 1–9. doi:10.1002/ppsc.201800533.

[37] P.S. Lemos, G.S. Silva, R.A. Roca, M. Assis, R. Torres-Mendieta, H. Beltrán-Mir, G. Mínguez-Vega, E. Cordoncillo, J. Andrés, E. Longo, Laser and electron beam-induced formation of Ag/Cr structures on Ag$_2$CrO$_4$, Physical Chemistry Chemical Physics. 21 (2019) 6101–6111. doi:10.1039/c8cp07263a.

802   [38] C.H.B. Ng, W.Y. Fan, Preparation of highly uniform 1-dimensional α-Ag$_2$WO$_4$

803   nanostructures with controllable aspect ratio and study of the growth mechanism,

804   CrystEngComm. 18 (2016) 8010–8019. doi:10.1039/c6ce01298a.

805   [39] P.F.S. Pereira, A.F. Gouveia, M. Assis, R.C. De Oliveira, I.M. Pinatti, M. Penha,

806   R.F. Gonçalves, L. Gracia, J. Andrés, E. Longo, ZnWO$_4$ nanocrystals: Synthesis,

807   morphology, photoluminescence and photocatalytic properties, Physical

808   Chemistry Chemical Physics. 20 (2018) 1923–1937. doi:10.1039/c7cp07354b.

809   [40] I.M. Pinatti, I.C. Nogueira, W.S. Pereira, P.F.S. Pereira, R.F. Gonçalves, J.A.

810   Varela, E. Longo, I.L.V. Rosa, Structural and photoluminescence properties of

811   Eu^{3+} doped α-Ag$_2$WO$_4$ synthesized by the green coprecipitation methodology,

812   Dalton Transactions. 44 (2015) 17673–17685. doi:10.1039/c5dt01997d.

813   [41] C.C. de Foggi, R.C. de Oliveira, M.T. Fabbro, C.E. Vergani, J. Andres, E. Longo,

814   A.L. Machado, Tuning the Morphological, Optical, and Antimicrobial Properties

815   of α-Ag$_2$WO$_4$ Microcrystals Using Different Solvents, Crystal Growth & Design.

816   17 (2017) 6239–6246. doi:10.1021/acs.cgd.7b00786.

817   [42] A.C.M. Tello, M. Assis, R. Menasce, A.F. Gouveia, V. Teodoro, N. Jacomaci,

818   M.A. Zaghete, J. Andrés, G.E. Marques, M.D. Teodoro, A.B.F. Da Silva, E.

819   Longo, Microwave-Driven Hexagonal-to-Monoclinic Transition in BiPO$_4$: An In-

820   Depth Experimental Investigation and First-Principles Study, Inorganic

821   Chemistry. 59 (2020) 7453–7468. doi:10.1021/acs.inorgchem.0c00181.

822   [43] R. Dovesi, A. Erba, R. Orlando, C.M. Zicovich-Wilson, B. Civalleri, L. Maschio,

823   M. Rérat, S. Casassa, J. Baima, S. Salustro, B. Kirtman, Quantum-mechanical

824   condensed matter simulations with CRYSTAL, Wiley Interdisciplinary Reviews:

825   Computational Molecular Science. 8 (2018) 1–36. doi:10.1002/wcms.1360.

826   [44] E. Aprà, E. Stefanovich, R. Dovesi, C. Roetti, An ab initio Hartree-Fock study of

827   silver chloride, Chemical Physics Letters. 186 (1991) 329–335. doi:10.1016/0009-
828   2614(91)90187-E.

829 [45] F. Corà, A. Patel, N.M. Harrison, R. Dovesi, C.R.A. Callow, An ab initio Hartree-
830   Fock study of the cubic and tetragonal phases of bulk tungsten trioxide, Journal of
831   the American Chemical Society. 118 (1996) 12174–12182.
832   doi:10.1021/ja961514u.

833 [46] L. Valenzano, F.J. Torres, K. Doll, F. Pascale, C.M. Zicovich-Wilson, R. Dovesi,
834   Ab initio study of the vibrational spectrum and related properties of crystalline
835   compounds; the case of $CaCO_3$ calcite, Zeitschrift Fur Physikalische Chemie. 220
836   (2006) 893–912. doi:10.1524/zpch.2006.220.7.893.

837 [47] K. Momma, F. Izumi, VESTA: A three-dimensional visualization system for
838   electronic and structural analysis, Journal of Applied Crystallography. 41 (2008)
839   653–658. doi:10.1107/S0021889808012016.

840 [48] R.A. Roca, J.C. Sczancoski, I.C. Nogueira, M.T. Fabbro, H.C. Alves, L. Gracia,
841   L.P.S. Santos, C.P. de Sousa, J. Andrés, G.E. Luz, E. Longo, L.S. Cavalcante,
842   Facet-dependent photocatalytic and antibacterial properties of α-Ag_2WO_4 crystals:
843   combining experimental data and theoretical insights, Catal. Sci. Technol. 5 (2015)
844   4091–4107. doi:10.1039/C5CY00331H.

845 [49] R.F. Egerton, P. Li, M. Malac, Radiation damage in the TEM and SEM, Micron.
846   35 (2004) 399–409. doi:10.1016/j.micron.2004.02.003.

847 [50] M. Assis, N.G. Macedo, T.R. Machado, M.M. Ferrer, A.F. Gouveia, E.
848   Cordoncillo, R. Torres-Mendieta, H. Beltrán-Mir, G. Mínguez-Vega, E.R. Leite,
849   J.R. Sambrano, J. Andrés, E. Longo, Laser/Electron Irradiation on Indium
850   Phosphide (InP) Semiconductor: Promising Pathways to In Situ Formation of
851   Indium Nanoparticles, Particle and Particle Systems Characterization. 35 (2018)

852   1–10. doi:10.1002/ppsc.201800237.

853   [51]   R.O. Torres-Mendieta, M.M. Teixeira, G. Mínguez-Vega, D. De Souza, Y.G.

854   Gobato, M. Assis, H. Beltrán-Mir, E. Cordoncillo, J. Andrés, M. Černík, E. Longo,

855   Toward Expanding the Optical Response of Ag_2CrO_4 and Bi_2O_3 by Their Laser-

856   Mediated Heterojunction, Journal of Physical Chemistry C. 124 (2020) 26404–

857   26414. doi:10.1021/acs.jpcc.0c08301.

858   [52]   V.N. Rai, S.N. Thakur, Physics and dynamics of plasma in laser-induced

859   breakdown spectroscopy, 2nd ed., Elsevier B.V., 2020. doi:10.1016/b978-0-12-

860   818829-3.00004-6.

861   [53]   P.M. Skarstad, S. Geller, $(W_4O_{16})^{8-}$ polyion in the high temperature modification

862   of silver tungstate, Mat. Res. Bull. 10(8), (1975) 791–799. doi:10.1016/0025-

863   5408(75)90193-2.

864   [54]   J. Andrés, L. Gracia, P. Gonzalez-Navarrete, V.M. Longo, W. Avansi, D.P.

865   Volanti, M.M. Ferrer, P.S. Lemos, F.A. La Porta, A.C. Hernandes, E. Longo,

866   Structural and electronic analysis of the atomic scale nucleation of Ag on α-

867   Ag_2WO_4 induced by electron irradiation, Scientific Reports. 4 (2014) 1–7.

868   doi:10.1038/srep05391.

869   [55]   L. Yang, J. Wang, Y. Wan, Y. Li, H. Xie, H. Cheng, H.J. Seo, Structure and

870   effective visible-light-driven photocatalytic activity of α-$NiMoO_4$ for degradation

871   of methylene blue dye, Journal of Alloys and Compounds. 664 (2016) 756–763.

872   doi:10.1016/j.jallcom.2015.10.037.

873   [56]   W. Zhu, X. Feng, Z. Wu, Z. Man, On the annealing mechanism in $PbWO_4$ crystals,

874   Physica B: Condensed Matter. 324 (2002) 53–58. doi:10.1016/S0921-

875   4526(02)01269-3.

876   [57]   O. Dulub, U. Diebold, G. Kresse, Novel Stabilization Mechanism on Polar

877   Surfaces: ZnO(0001)-Zn, Physical Review Letters. 90 (2003) 4.

878   doi:10.1103/PhysRevLett.90.016102.

879 [58] A. Barbier, G. Renaud, A. Stierle, The NiO (111)-(1 × 1) surface, Surface Science.

880   402–404 (1998) 757–760. doi:10.1016/S0039-6028(97)01020-0.

881 [59] C. Ren, R. Yang, Y. Li, H. Wang, Modulating of facets-dependent oxygen

882   vacancies on ceria and its catalytic oxidation performance, Research on Chemical

883   Intermediates. 45 (2019) 3019–3032. doi:10.1007/s11164-019-03776-6.

884 [60] H. He, S. Xue, Z. Wu, C. Yu, K. Yang, G. Peng, W. Zhou, D. Li, Sonochemical

885   fabrication, characterization and enhanced photocatalytic performance of

886   Ag_2S/Ag_2WO_4 composite microrods, Cuihua Xuebao/Chinese Journal of

887   Catalysis. 37 (2016) 1841–1850. doi:10.1016/S1872-2067(16)62515-9.

888 [61] F.Y. Xie, L. Gong, X. Liu, Y.T. Tao, W.H. Zhang, S.H. Chen, H. Meng, J. Chen,

889   XPS studies on surface reduction of tungsten oxide nanowire film by Ar^+

890   bombardment, Journal of Electron Spectroscopy and Related Phenomena. 185

891   (2012) 112–118. doi:10.1016/j.elspec.2012.01.004.

892 [62] A. Turkovič, D.L. Fox, J.F. Scott, S. Geller, G.F. Ruse, High temperature Raman

893   spectroscopy of silver tetratungstate, $Ag_8W_4O_{16}$, Materials Research Bulletin. 12

894   (1977) 189–195. doi:10.1016/0025-5408(77)90163-5.

895 [63] S.K. Gupta, K. Sudarshan, P.S. Ghosh, S. Mukherjee, R.M. Kadam, Doping-

896   Induced Room Temperature Stabilization of Metastable β-Ag_2WO_4 and Origin of

897   Visible Emission in α- And β-Ag_2WO_4: Low Temperature Photoluminescence

898   Studies, Journal of Physical Chemistry C. 120 (2016) 7265–7276.

899   doi:10.1021/acs.jpcc.6b00078.

900 [64] I.M. Pinatti, G.R. Fern, E. Longo, T.G. Ireland, P.F.S. Pereira, I.L.V. Rosa, J.

901   Silver, Luminescence properties of α-Ag_2WO_4 nanorods co-doped with Li^+ and

902   Eu^{3+} cations and their effects on its structure, Journal of Luminescence. 206 (2019)

903   442–454. doi:10.1016/j.jlumin.2018.10.104.

904   [65]   A.C. Catto, T. Fiorido, É.L.S. Souza, W. Avansi, J. Andres, K. Aguir, E. Longo,

905   L.S. Cavalcante, L.F. da Silva, Improving the ozone gas-sensing properties of

906   CuWO$_4$ nanoparticles, Journal of Alloys and Compounds. 748 (2018) 411–417.

907   doi:10.1016/j.jallcom.2018.03.104.

908   [66]   A.C. Catto, L.F.D. Silva, M.I.B. Bernardi, S. Bernardini, K. Aguir, E. Longo, V.R.

909   Mastelaro, Local Structure and Surface Properties of Co$_x$Zn$_{1-x}$O Thin Films for

910   Ozone Gas Sensing, ACS Applied Materials and Interfaces. 8 (2016) 26066–

911   26072. doi:10.1021/acsami.6b08589.

912   [67]   L.S. Cavalcante, M.A.P. Almeida, W. Avansi, R.L. Tranquilin, E. Longo, N.C.

913   Batista, V.R. Mastelaro, M.S. Li, Cluster coordination and photoluminescence

914   properties of α-Ag$_2$WO$_4$ microcrystals, Inorganic Chemistry. 51 (2012) 10675–

915   10687. doi:10.1021/ic300948n.

916   [68]   M.M. Teixeira, Y.G. Gobato, L. Gracia, L.F. da Silva, W. Avansi, M. Assis, R.C.

917   de Oliveira, G.A. Prando, J. Andrés, E. Longo, Towards a white-emitting phosphor

918   Ca$_{10}$V$_6$O$_{25}$ based material, Journal of Luminescence. 220 (2020) 116990.

919   doi:10.1016/j.jlumin.2019.116990.

920   [69]   L.F. Da Silva, A.C. Catto, W. Avansi, A. Mesquita, L.J.Q. Maia, O.F. Lopes, M.S.

921   Li, M.L. Moreira, E. Longo, J. Andrés, V.R. Mastelaro, Unveiling the efficiency

922   of microwave-assisted hydrothermal treatment for the preparation of SrTiO$_3$

923   mesocrystals, Physical Chemistry Chemical Physics. 21 (2019) 22031–22038.

924   doi:10.1039/c9cp02893e.

925   [70]   S. Yamazoe, Y. Hitomi, T. Shishido, T. Tanaka, XAFS study of tungsten L$_1$- And

926   L$_3$-edges: structural analysis of WO$_3$ species loaded on TiO$_2$ as a catalyst for photo-

927   oxidation of NH$_3$, Journal of Physical Chemistry C. 112 (2008) 6869–6879.

928   doi:10.1021/jp711250f.

929   [71] G. Poirier, F.C. Cassanjes, Y. Messaddeq, S.J.L. Ribeiro, A. Michalowicz, M.

930   Poulain, Local order around tungsten atoms in tungstate fluorophosphate glasses

931   by X-ray absorption spectroscopy, Journal of Non-Crystalline Solids. 351 (2005)

932   3644–3648. doi:10.1016/j.jnoncrysol.2005.08.038.

933   [72] D.Wood, J.Tauc, Weak Absorption Tails in Amorphous Semiconductors, 5(8)

934   (1972), 3144–3151. doi:10.1103/physrevb.5.3144.

935   [73] B. Philips-Invernizzi, Bibliographical review for reflectance of diffusing media,

936   Optical Engineering. 40 (2001) 1082. doi:10.1117/1.1370387.

937   [74] L. Yang, B. Kruse, Revised Kubelka–Munk theory I Theory and application,

938   Journal of the Optical Society of America A. 21 (2004) 1933.

939   doi:10.1364/josaa.21.001933.

940   [75] A. Sreedevi, K.P. Priyanka, K.K. Babitha, N. Aloysius Sabu, T.S. Anu, T.

941   Varghese, Chemical synthesis, structural characterization and optical properties of

942   nanophase α-Ag$_2$WO$_4$, Indian Journal of Physics. 89 (2015) 889–897.

943   doi:10.1007/s12648-015-0664-1.

944   [76] M. Li, T. Takei, Q. Zhu, B. Kim, J. Li, Morphology Tailoring of ZnWO 4

945   Crystallites / Architectures and Photoluminescence of the Doped RE^{3+} Ions (RE =

946   Sm , Eu , Tb , and Dy), Inorganic Chemistry. 58 (2019) 9432–9442.

947   doi:10.1021/acs.inorgchem.9b01271.

948   [77] R. Alvarez-Roca, A.F. Gouveia, C.C. De Foggi, P.S. Lemos, L. Gracia, L.F. Da

949   Silva, C.E. Vergani, M. San-Miguel, E. Longo, J. Andrés, Selective Synthesis of

950   α-, β-, and γ-Ag$_2$WO$_4$ Polymorphs: Promising Platforms for Photocatalytic and

951   Antibacterial Materials, Inorganic Chemistry. 60 (2021) 1062–1079.

952   doi:10.1021/acs.inorgchem.0c03186.

953

954 **FIGURE CAPTIONS**
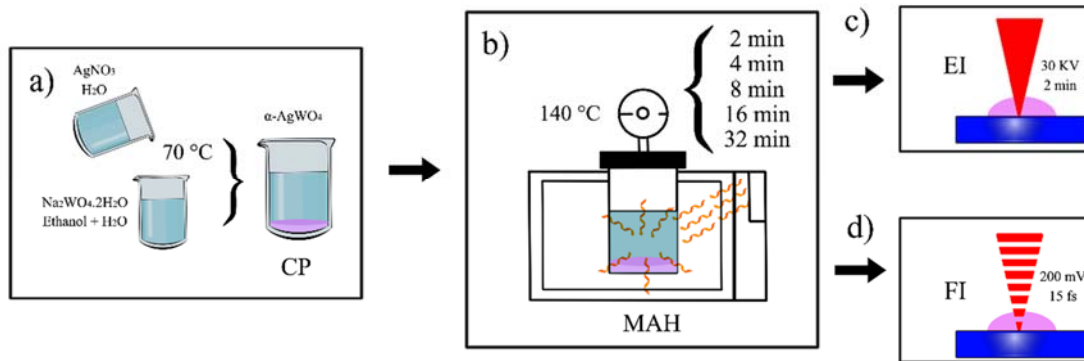
955

956 **Figure 2.** Scheme with steps of a) Synthesis by CP method, b) Treatment by MAH
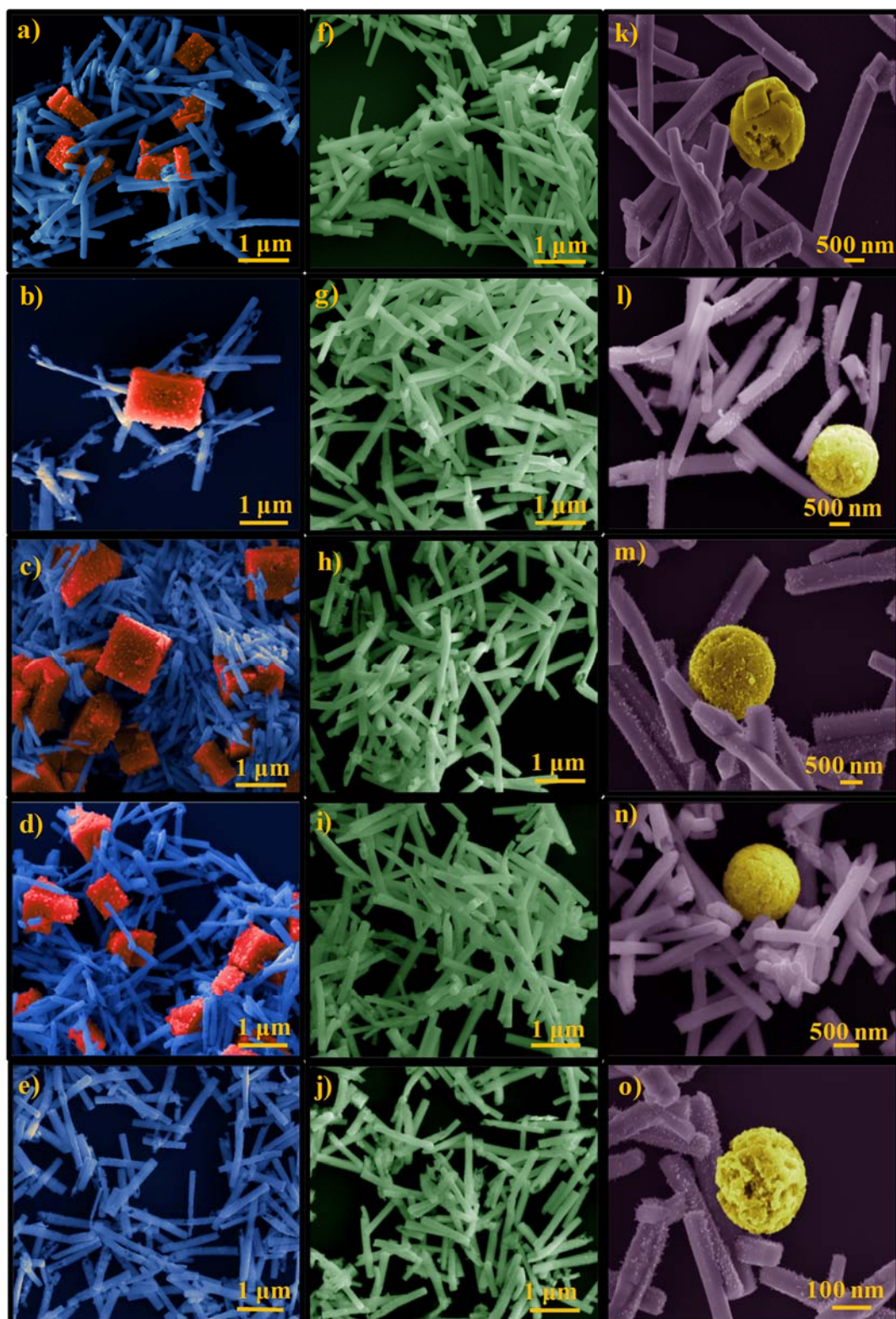
957 method, c) Electron beam irradiation, and d) Femtosecond laser irradiation; to obtain α-
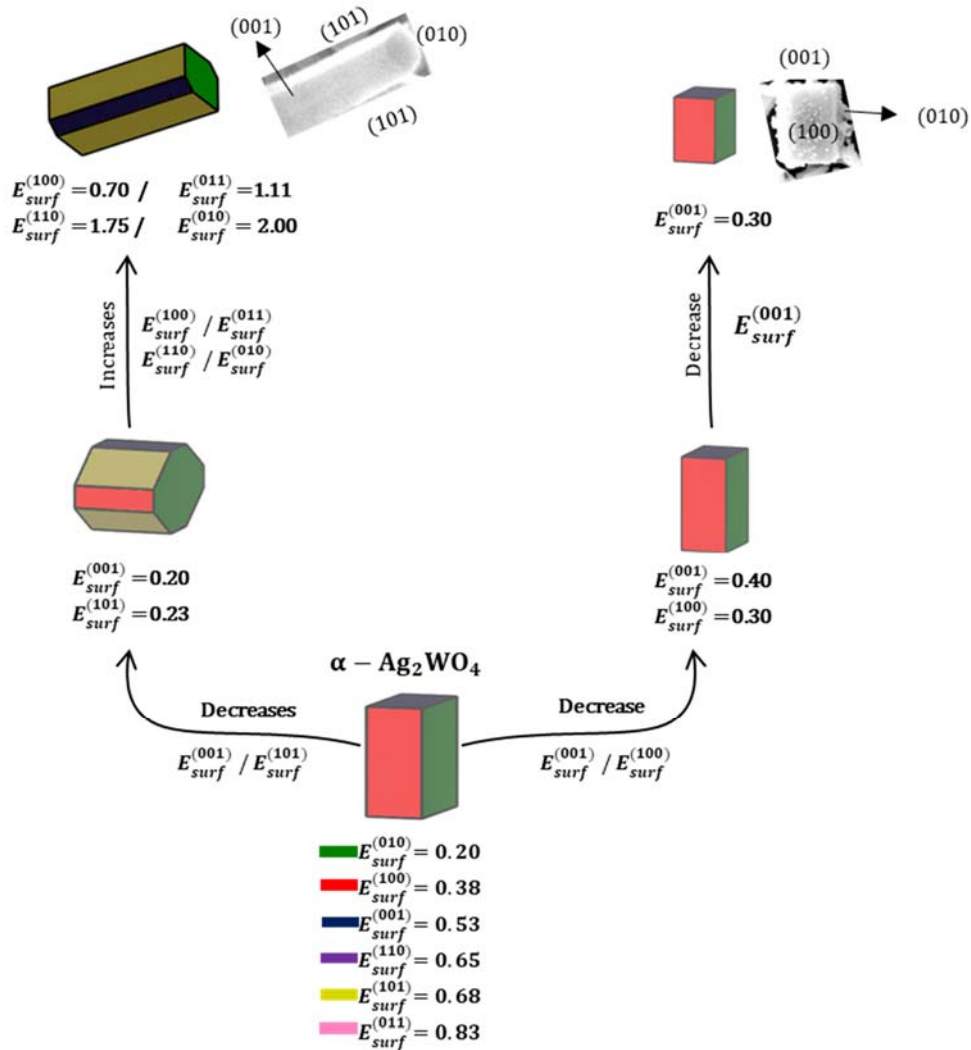
958 Ag$_2$WO$_4$ samples.

959

960

961

Figure 2. FE-SEM images of α-Ag$_2$WO$_4$ particles of MAH, EI, and FI. (a-e) heterogeneous morphology obtained after treatment with MAH at different treatment times (2, 4, 8, 16, and 32 min) with the cubes highlighted in orange color and the rods-like in blue color; (f-j) rods-like with homogeneous morphology after EI indicated by

Figure 3. Wulff construction for α–Ag₂WO₄. For comparison, experimental FE-SEM images are shown. E_{surf} values are given in Jm^{-2}.
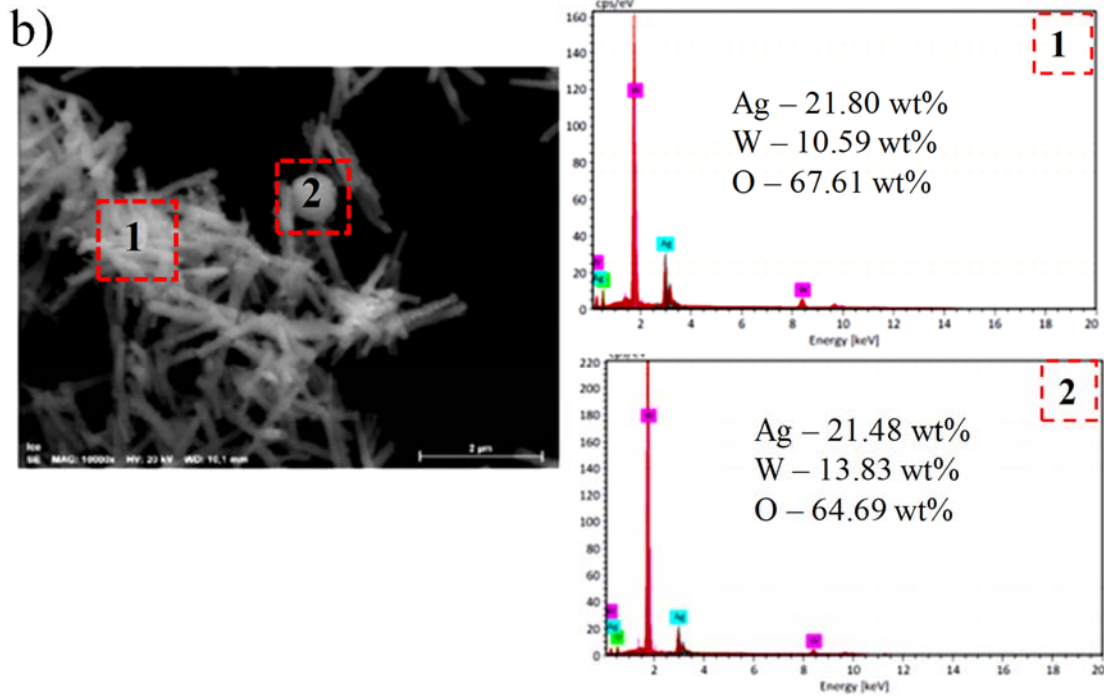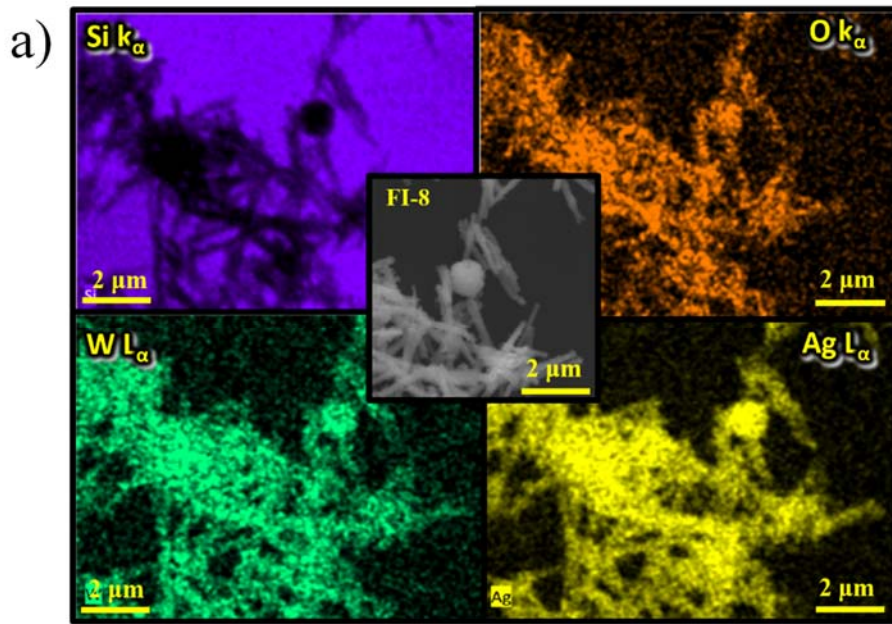
Figure 4. a) EDS elemental mapping of the FI-8 sample of Si Kα, O Kα, W Lα, and Ag Lα. b) FI-8 sample analyzed by EDS, highlighting the rod- and sphere-like morphologies. c) Rod-like region 1 and d) Sphere-like region 2.

985
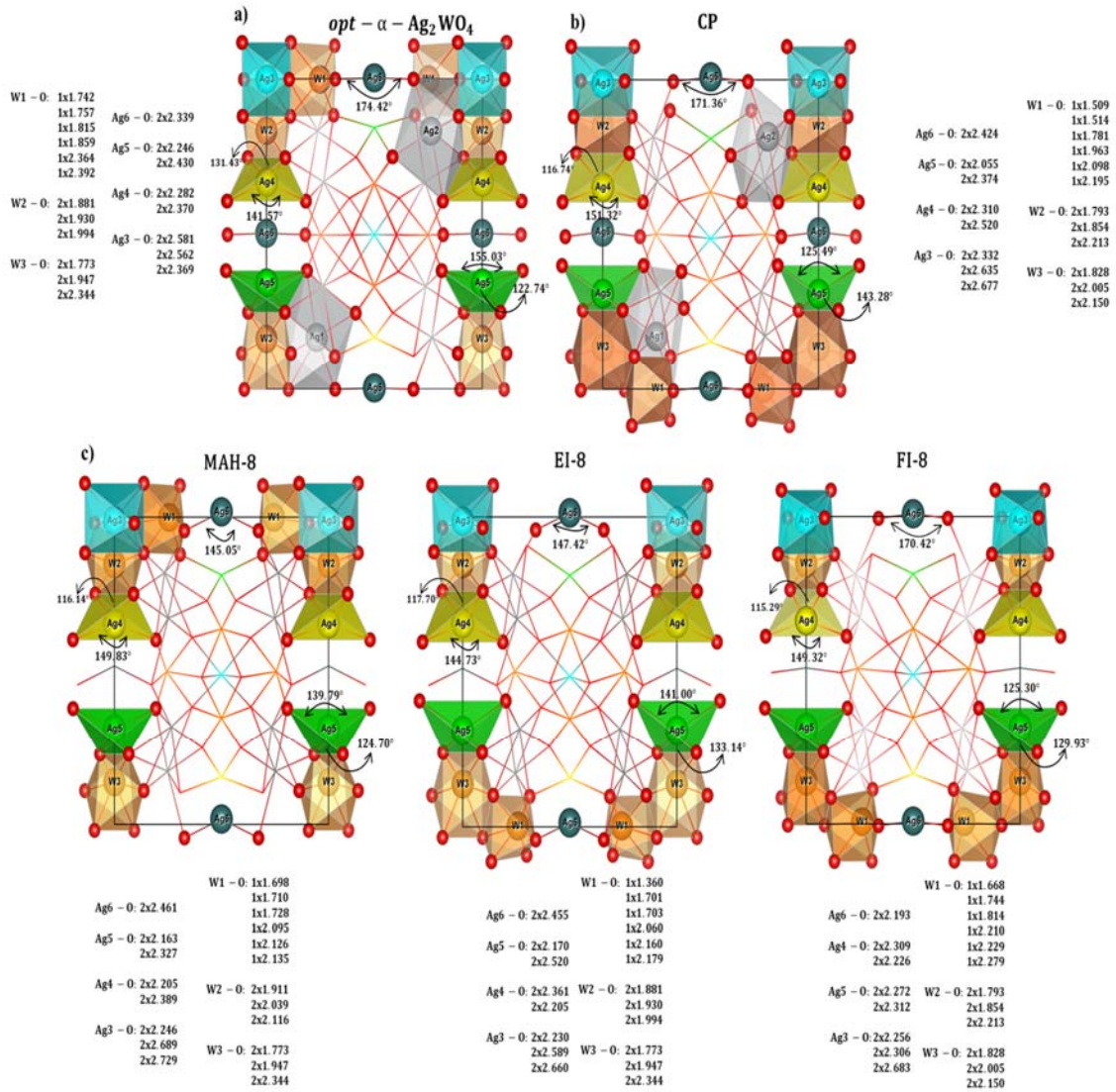
Figure 5. Geometry of a) $opt - \alpha$-Ag$_2$WO$_4$, b) CP, and c) irradiated (MAH-8, EI-8, and

FI-8) structures.

988

989

990
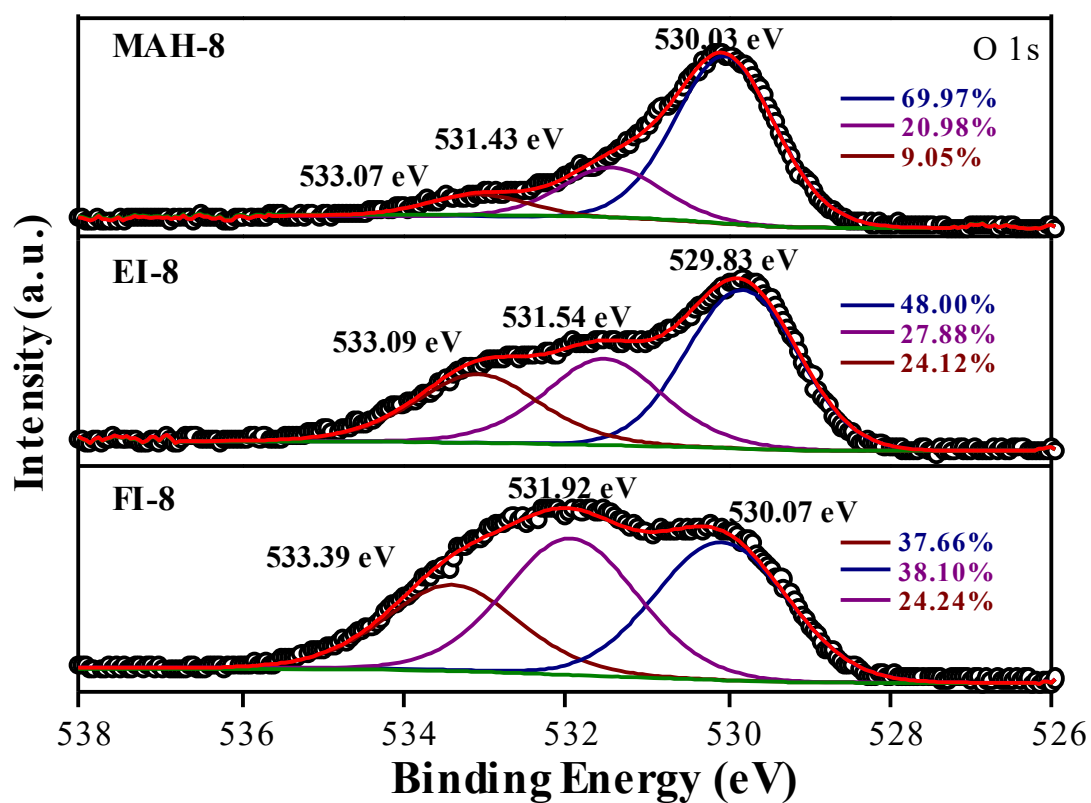
991

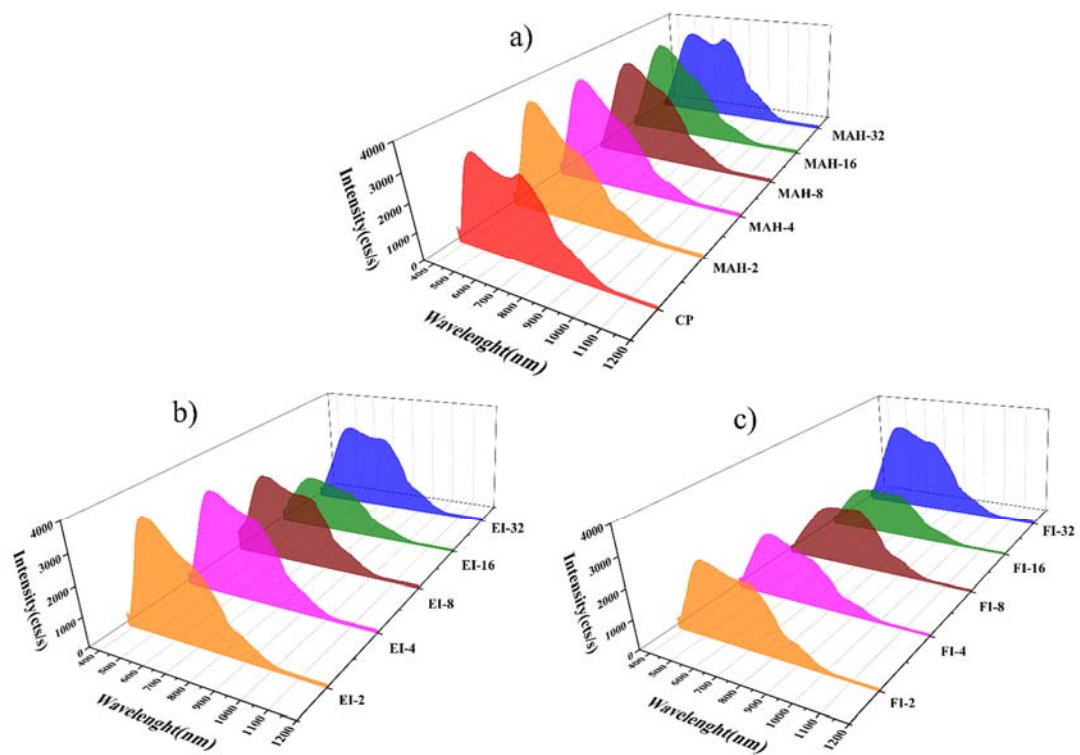992 **Figure 6.** High-resolution XPS spectra of O *1s* for the MAH-8, EI-8, and FI-8 samples.

993

994

995

996
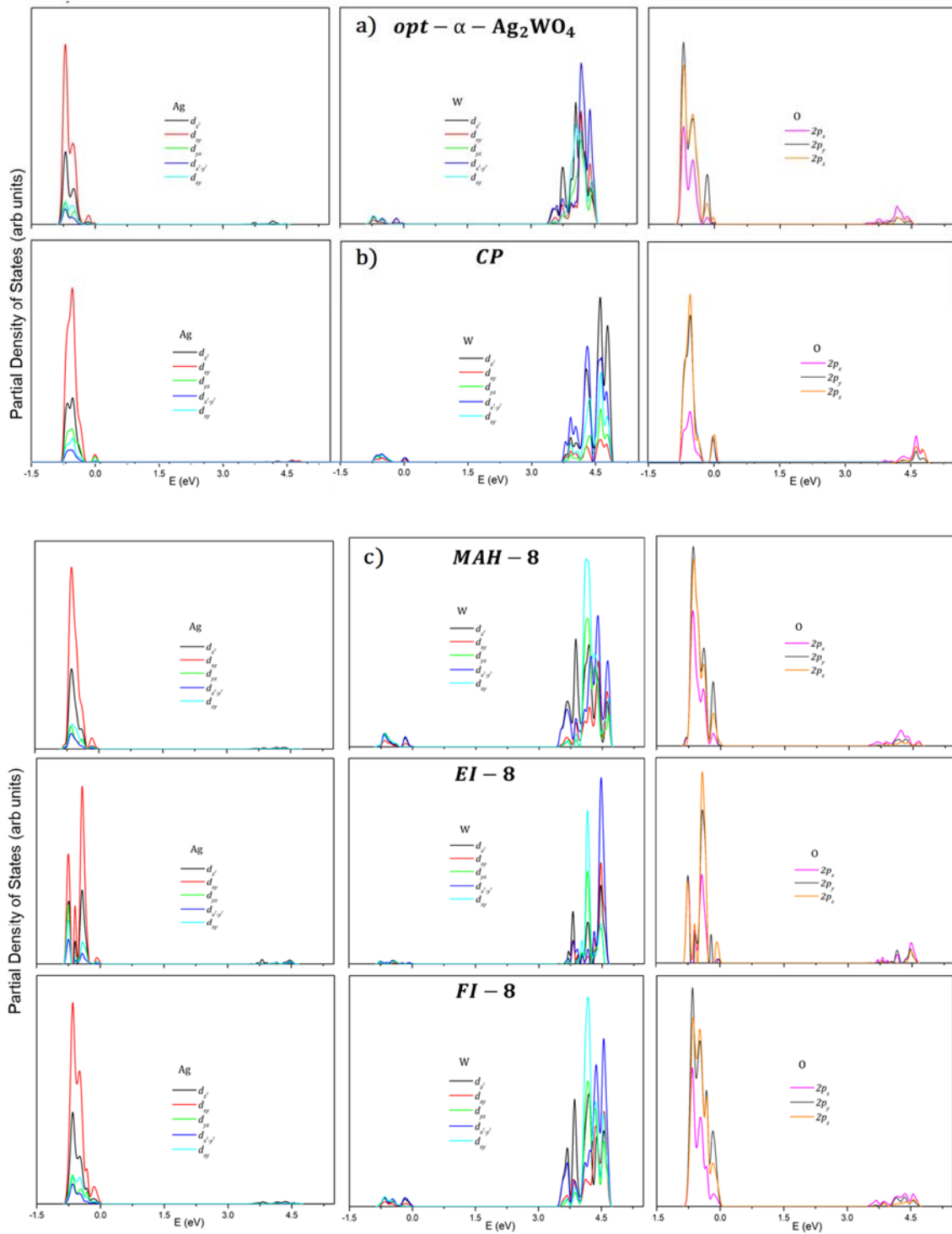
Figure 7. Partial density of states projected on the *4d*, *5d* and *2p* orbitals of Ag, W, and O atoms, respectively, for a) *opt–α*-Ag2WO4, b) CP, and c) irradiated (MAH-8, EI-8, and FI-8) samples.

Figure 8. PL spectra of the samples obtained by a) the CP method, treated with MAH and irradiated by b) EI and c) FI.

1010

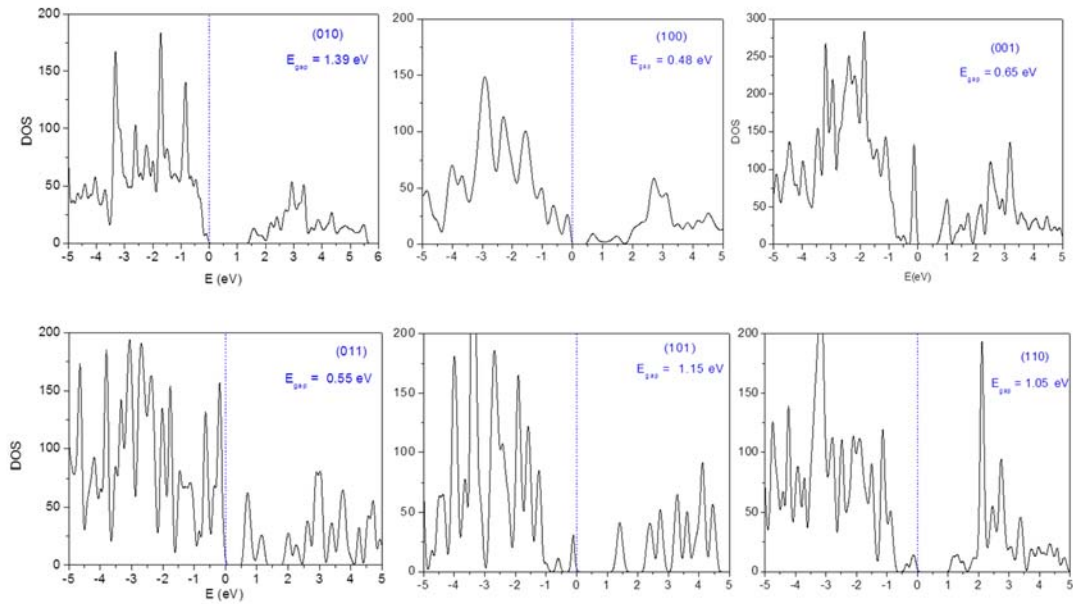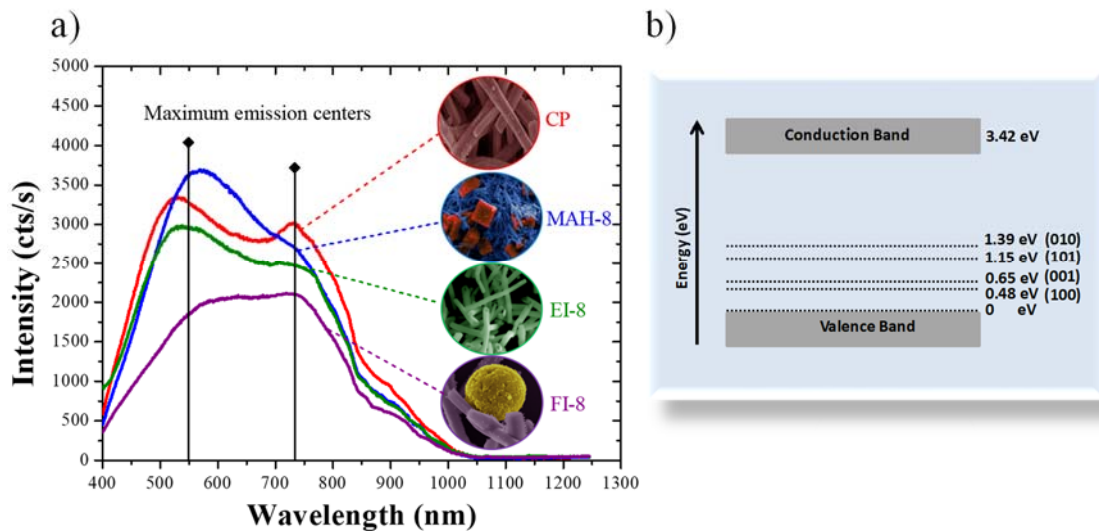1011 **Figure 9.** Total density of states for the (010), (100), (001), (011), (101), and (110)

1012 surfaces of α-Ag$_2$WO$_4$.

1013

1014

1015

1016

1017 **Figure 10.** (a) PL spectra and maximum emission centers of the CP, MAH-8, EI-8, and

1018 FI-8 samples. (b) Comparative diagram of the band gap value of the optimized structure

1019 (3.42 eV) and band gap values for (100), (010), (001), and (101) surfaces.